Energy & Environmental Science

ROYAL SOCIETY OF CHEMISTRY

PAPER

View Article Online
View Journal

Cite this: DOI: 10.1039/d6ee00129g

Integrating atomic scale catalyst design with transport engineering for stable and efficient CO_2 electrolysis to CO in a membrane electrode assembly

Zahra Teimouri,[a] Mahtab Masouminia,[a] Ashkan Irannezhad,[a] Reza Eslami,[a] Joseph Deering,[b] Navid Noor,[a] Shunquan Tan,[a] Amirhossein Foroozan Ebrahimy,[a] Shayan Angizi,[a] Sung-Fu Hung[c] and Drew Higgins*[a]

Electrochemical CO_2 reduction (CO_2R) offers a promising approach to for decarbonizing chemical manufacturing through production of carbon-neutral fuels. However, insufficient performance and instability of the membrane electrode assembly (MEA) reactors limit the commercial viability, with both metrics directly impacted by the CO_2R catalysts. Here we develop atomically dispersed nickel–nitrogen–carbon (NiNC) catalysts through a scalable synthesis approach that enables controlled dispersion of isolated Ni active sites using two different carbon supports. When using carbon nanotubes as a support, the resulting NiNCNT electrode achieves a partial current density towards CO of 558 mA cm^{-2} with 92% faradaic efficiency towards CO at a cell voltage of 3.2 V and an energy efficiency of 39% at a total current density of 607 mA cm^{-2}. The MEA demonstrated stable operation at 100 mA cm^{-2} over 210 hours, outperforming previously reported NiNC catalysts. Focused ion beam-scanning electron microscopy (FIB-SEM) tomography reveals the critical role of catalyst support architecture in governing electrode performance. COMSOL Multiphysics simulations using the 3D reconstructed images of the catalyst layers from FIB-SEM tomography demonstrated that the higher CO_2R performance of the NiNCNT electrode is due to improved CO_2 diffusion and a more uniform current-density distribution compared to the NiNCB electrode prepared with carbon black as the support. These results highlight the key role of catalyst-layer morphology in governing the CO_2R performance of the two catalysts, despite their similar Ni and N loadings. The stability and performance of the NiNCNT compared favourably to the state-of-the-art Ag-based catalysts, while bottom-up cost analysis estimated the projected purchase cost of the NiNCNT catalyst to be $589 USD per kg, substantially lower than $1900 USD per kg estimated for Ag-based catalysts, highlighting its potential for scalable and economically viable CO_2R electrolyzers.

Received 7th January 2026,
Accepted 7th May 2026

DOI: 10.1039/d6ee00129g

rsc.li/ees

Broader context

Converting CO_2 into value-added chemicals using renewable electricity offers a promising route toward sustainable chemical manufacturing. CO is a key intermediate for producing fuels and chemicals through CO_2 electrochemical reduction (CO_2R). However, a critical bottleneck plaguing the commercial viability of CO_2 electrolyzers to CO production is the low carbon utilization, efficiency and stability under industrially relevant operating conditions in membrane electrode assembly (MEA) reactors, which is the most commercially viable reactor configuration. This work demonstrates how rationally engineering the synthesis method enables precise control over the spatial distribution and local coordination of active sites in atomically dispersed MNC (transition metal sites coordinated by nitrogen within a carbonaceous framework) catalysts. By combining three-dimensional FIB-SEM tomography with Multiphysics modeling, we directly correlate the architecture of the catalyst layer with CO_2R performance and stability in MEA, highlighting design metrics for scalable, high-performance MNC electrodes. The resulting electrode was compared favorably with Ag electrodes (benchmark catalyst for CO_2R to CO). Our tomography-informed numerical modeling framework establishes a transferable workflow that links 3D electrode architecture to mass transport, providing practical guidance for optimizing porous-electrode designs across electrochemical devices. In parallel, the cost analysis implemented in this work identifies actionable cost levers such as the catalyst support and synthesis method, which extend beyond CO_2R electrolyzers to electrified chemical manufacturing more broadly.

[a] *Department of Chemical Engineering, McMaster University, Hamilton, ON, Canada. E-mail: higgid2@mcmaster.ca*
[b] *Canadian Centre for Electron Microscopy, Hamilton, ON, Canada*
[c] *Department of Applied Chemistry and Centre for Emergent Functional Matter Science, National Yang Ming Chiao Tung University, Hsinchu 300, Taiwan*

Introduction

Electrochemical CO_2 reduction (CO_2R) can store renewable electricity in the form of chemical bonds, providing a route to reduce emissions across various industrial sectors.[1–3] Continuous and rapid decline in the cost of clean electricity is rendering electricity-driven conversion technologies progressively more cost-competitive. At the same time, global energy-related CO_2 emissions remain very large ($\approx$37.8 Gt in 2024), underscoring an urgent need to reduce carbon emissions. Together, these trends position CO_2R as a timely technological pathway to convert CO_2 into valuable chemicals and fuels and place CO_2-utilization at the center of carbon-circular manufacturing strategies.[4,5] CO_2R can yield a variety of products including C_1 (carbon monoxide, syngas (CO/H_2 mixture), formate, and methane), and C_{2+} products (ethylene, ethanol, propanol, *etc.*) depending on the structure and composition of the electrocatalyst,[6,7] as well as the local reaction environment.[8] CO, a key feedstock for industrial processes like Fischer–Tropsch synthesis, is the most economically promising CO_2R product due to the high selectivity and simpler separation process compared to C_{2+} products.[9–12] Despite considerable efforts toward commercialization of the low-temperature (<80 °C) CO_2R electrolyzers for CO production, challenges remain, including low faradaic efficiencies towards CO due to the competing hydrogen evolution reaction (HER) at high current densities (>500 mA cm^{-2}) and low electrolyzer stability, which still falls short of the industrial benchmarks of up to 50 000 hours.[4,13] The stability of CO_2R systems is influenced by the chemical and mechanical robustness of various components, including the electrocatalysts, ionomers, and electrolyte membranes, with the electrocatalyst being recognized as a primary source of performance loss over time.[14,15]

Ag and Au are considered the state-of-the-art catalysts for CO_2R to CO due to their high selectivity and activity, but their high cost limits the commercial viability.[16] As an alternative, catalysts consisting of atomically dispersed transition metal sites (such as Ni, Co, or Fe) coordinated by nitrogen within a carbonaceous framework (MNC) have gained significant attention due to the tunable physicochemical properties and lower costs compared to the Au and Ag-based catalysts.[16–18] However, a rigorous production-scale technoeconomic comparison demonstrating this cost advantage is generally lacking. Such an analysis would pinpoint dominant cost drivers such as the price of metal precursors, synthesis yield, energy/operating costs, and selection of the catalyst support, which can be translated into concrete design rules to guide scalable catalyst synthesis for CO_2R electrolyzers. The primary synthesis method for MNC catalysts is through physical/mechanical mixing of the metal and nitrogen precursors with a carbon support, followed by pyrolysis at high temperatures (>500 °C).[16,19] During the pyrolysis step, the transition metal atoms have the tendency to agglomerate to decrease their surface free energy, which enhances H_2 selectivity due to the propensity of metallic clusters to favour the HER.[20,21] On the other hand, non-uniform distribution of the nitrogen coordination sites throughout the catalyst structure can result when there is insufficient mixing of the catalyst precursors, resulting in a spatially heterogeneous distribution of the M–N_x active sites that negatively affects the electrode performance.[16,19,22] Despite numerous reports on the application of MNC catalysts in CO_2R, the impact of synthesis method, in particular the spatial distribution of the N precursor relative to the Ni precursor and carbon support, remains poorly understood.

Physicochemical properties of the carbon support (*e.g.*, surface area, pore size distribution and hydrophobicity) used during the synthesis also play a critical role in dictating the capability of MNC catalysts to meet the performance demands required for the CO_2R scale-up: particularly, current densities (j) exceeding 200 mA cm^{-2}, faradaic efficiencies (FE) towards CO exceeding 90%, and operational cell voltages less than 3 V in a MEA.[23] To achieve these targets, existing literature has mainly focused on increasing the number of active sites or the intrinsic activity of each active site through engineering Ni–N coordination. These studies often overlook the important role of the catalyst morphology and resulting electrode structure towards the performance of CO_2R electrolyzers at high current density where mass transport is a critical consideration. Engineering the porosity of the catalyst layer through rational selection of the carbon support used during synthesis offers an effective approach to improve CO_2 transport.[24] Fu *et al.*[25] demonstrated that NiNC electrodes synthesized using biochar with a hierarchical porous structure as the carbon support improved the partial current density towards CO, which originates from increased CO_2 transport, compared to the electrodes prepared using CB and CNT as the catalyst supports in a MEA electrolyzer using vapour-fed CO_2 at comparable cell voltages. Beyond nanoscale porosity within the individual carbon particles, the mesoscale interparticle porosity critically controls the transport of reactants, ions and products through the catalyst layer. Well-connected pores can shorten gas-phase diffusion pathways and reduce tortuosity, increasing the effective CO_2 diffusivity to buried active sites to maintain high local CO_2 partial pressures even at high current densities. Therefore, engineering the interparticle porosity offers a direct lever to improve mass transport, selectivity and stability in the MEA electrolyzers for CO_2R, which is lacking in the literature.[26,27]

In this work, we introduce a scalable synthesis method that controls nitrogen-precursor impregnation during synthesis to maximize the concentration of Ni–N_x active sites, yielding NiNC catalysts that provide partial current density towards CO of 558 mA cm^{-2} at a cell voltage of 3.2 V in a MEA reactor with a record-setting energy efficiency of 39% towards CO. We sought to understand the origins of such high performance compared to the state-of-the-art NiNC and Ag catalysts by using FIB-SEM tomography to reconstruct the three-dimensional (3D) morphology of the catalyst layers prepared using either CNTs or CB with distinct morphologies as catalyst supports. This approach enables quantitative analysis of the interparticle porosity and structural connectivity in the gas diffusion electrode (GDE). The 3D-reconstructed geometries were directly incorporated into COMSOL Multiphysics simulations, enabling

modeling of the CO_2 transport based on an actual catalyst layer architecture, rather than idealized geometries. The simulations revealed that the interconnected morphology of the NiNCNT catalyst layer facilitated CO_2 diffusion and promoted a uniform current density distribution compared to the tortuous structure of the NiNCB catalyst layer. The production cost of the NiNCNT catalyst was also estimated as \$589 USD per kg, providing an economically feasible alternative for Ag-based catalysts, which range from \$1800 to 2000 USD per kg.

Catalyst synthesis

We employed two distinct routes for the synthesis of NiNC catalysts: (a) carbon support (CB or CNT) was impregnated with a nickel nitrate precursor and glucose, followed by drying and physically mixing with melamine using a mortar and pestle before pyrolysis; (b) simultaneous wetness impregnation of the nickel nitrate precursor, glucose and melamine onto the carbon support, allowing chelation of the hydroxyl groups in glucose with the hydrated Ni ions,[19] and π–π/H-bond interactions of melamine with the carbon support. This was followed by drying and pyrolysis (Scheme 1). Catalysts prepared from the first method are denoted as NiNX-phys Y, and those from the second methodology as NiNX-sim Y, where X stands for CNTs or CB and Y represents the pyrolysis temperature. Melamine was selected as the nitrogen precursor due to its high N/C ratio and relatively lower cost compared to other N–C building blocks such as dicyandiamide (DCDA) and polyaniline (PANI).[28,29] In our synthesis method, the Ni–glucose complexes likely start to decompose at elevated temperature (>600 °C), and the resulting Ni atoms can potentially coordinate with surrounding CN_x sites that are formed during the carbonization of melamine to form Ni–N_x motifs, as suggested previously.[19,30] Thus, glucose presumably plays a key role in sequestration of Ni species, while melamine mainly contributes to the formation of the N-rich carbon framework that anchors Ni–N_x moieties.

CO_2R performance results

The CO_2R performance of the NiNC electrodes was investigated in an MEA, with additional details on the experimental set-up provided in the Methods section. We investigated the impact of pyrolysis temperature on the CO_2R performance of the synthesized electrodes (Fig. 1a–c). The NiNCNT-sim 800 °C electrode (Fig. 1b) exhibits higher j_{CO} than the NiNCNT-sim 700 °C (Fig. 1a) and NiNCNT-sim 900 °C electrodes (Fig. 1c) at different cell voltages that were tested, reaching a j_{CO} of 558 mA cm^{-2} at 3.2 V with a FE_{CO} of 92%. We also studied how the catalyst synthesis method controls the CO_2R performance of the electrodes in an MEA. The NiNCNT-phys electrodes (Fig. 1d–f) provided a lower j_{total} and j_{CO} compared to the catalysts prepared using the simultaneous wetness impregnation method (NiNCNT-sim) at all tested cell voltages (Fig. 1a–c and 2a).

The operational stability of the best performing electrode (NiNCNT-sim 800 °C) was evaluated using chronopotentiometry measurements at a constant current density of 100 mA cm^{-2}, with the results shown in Fig. 2b. The stability test was performed using a more dilute electrolyte (0.1 $MKHCO_3$) to mitigate the performance degradation arising from salt precipitation. It has been reported that reducing the bulk K^+ concentration in the anolyte diminishes cation migration toward the cathode. As a result, potassium accumulation at the cathode can remain below the solubility limit of K_2CO_3 for longer, thereby delaying salt precipitation.[15] The CO_2R

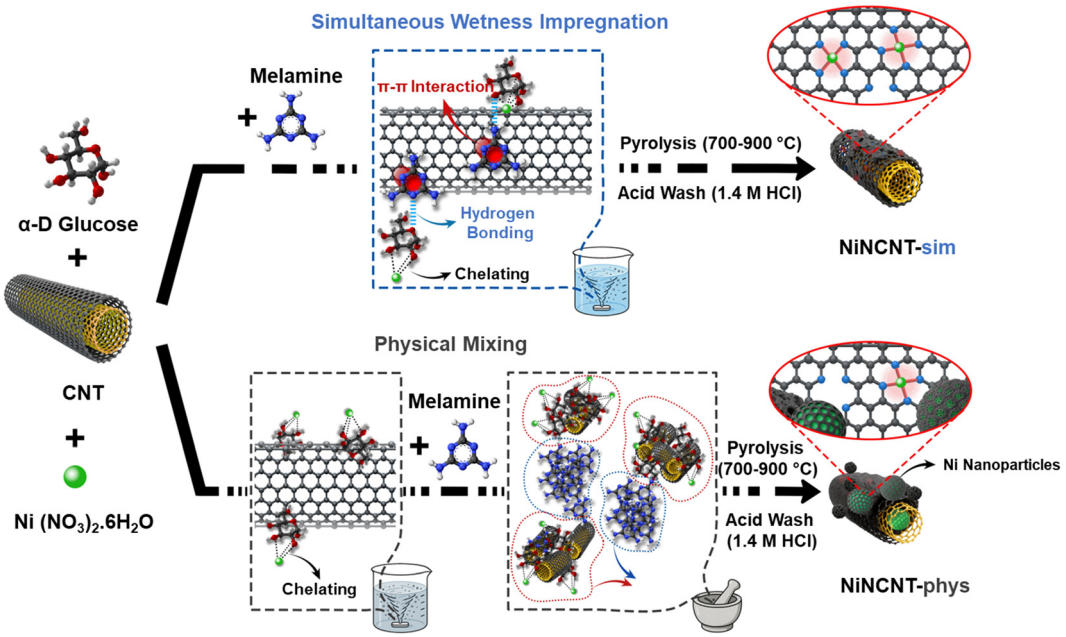

Scheme 1 Schematic illustration of the synthesis process for simultaneous wetness impregnation and physical mixing of melamine for the synthesis of the NiNCNT catalysts.

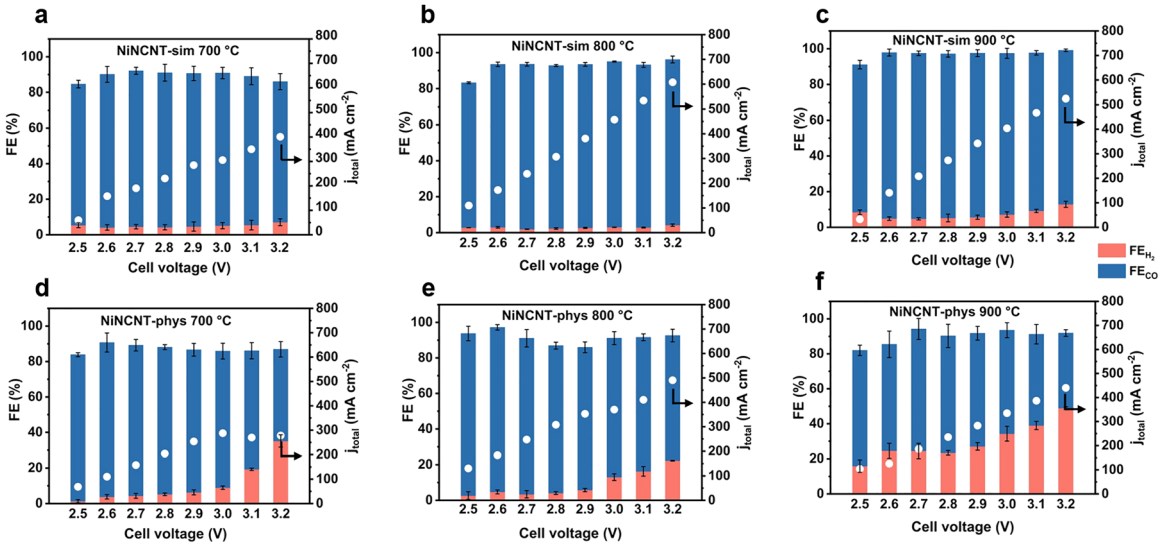

Fig. 1 CO_2R performances of: (a) NiNCNT-sim 700 °C, (b) NiNCNT-sim 800 °C, (c) NiNCNT-sim 900 °C, (d) NiNCNT-phys 700 °C, (e) NiNCNT-phys 800 °C, (f) NiNCNT-phys 900 °C electrodes. The CO_2R performance tests were conducted in a MEA using 0.5 M $KHCO_3$ as an anolyte. The error bars in (a)–(f) correspond to the standard deviation of three independent measurements.

performance was largely retained over 210 hours of electrolysis. Particularly, less than a 5% change in the cell voltage and FE_{CO} was observed throughout the operation. This stability is over three times longer than the maximum of 70 hours previously reported in the literature for state-of-the-art NiNC catalysts tested in a MEA.[23,31–33] Compared to previous NiNC electrodes tested in a MEA with current densities >500 mA cm^{-2}, the NiNCNT-sim 800 °C electrode provides the highest energy efficiency reported to date, reaching ~39% (Table S1 and Fig. 2c). We also compared the CO_2R performance and stability of the NiNCNT-sim 800 °C electrode with the state-of-the-art Ag electrodes operating in a MEA (Fig. 2d and Table S1).[34–39] Compared with Ag electrodes operating between 3.2–3.6 V, our best performing electrode (NiNCNT-sim 800 °C) achieved

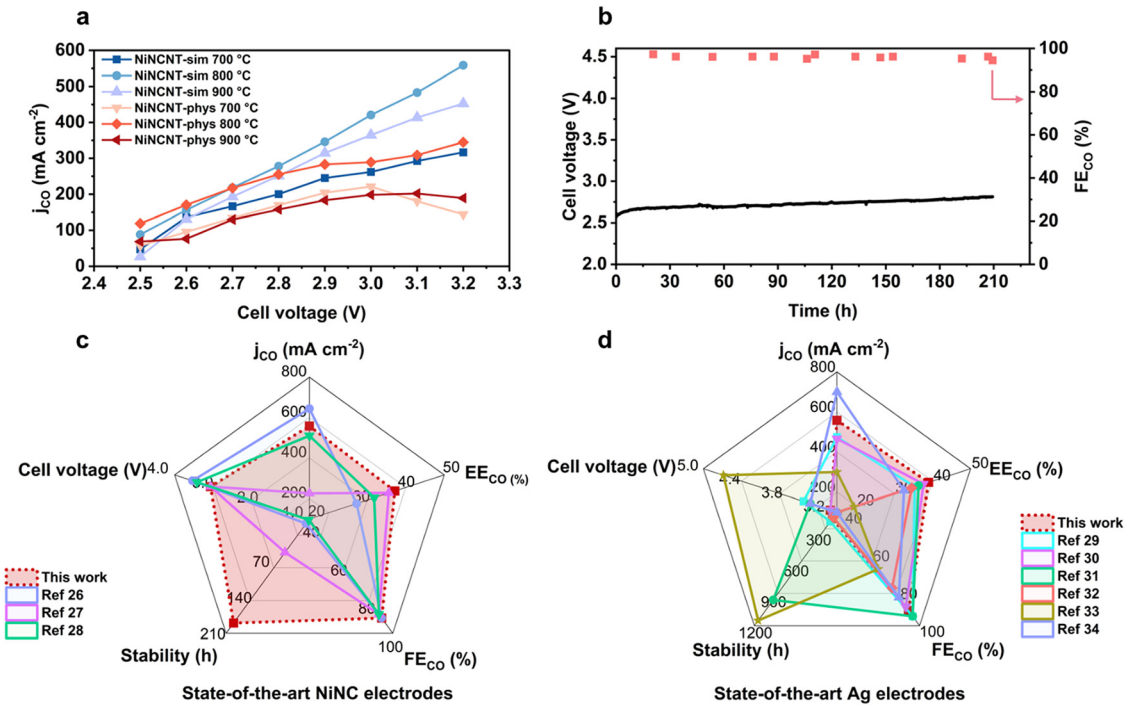

Fig. 2 (a) Effect of pyrolysis temperature and catalyst preparation method on the j_{CO}, (b) stability of the NiNCNT-sim 800 °C electrode in a MEA at applied current density of 100 mA cm^{-2} using 0.1 M $KHCO_3$ electrolyte, comparison of the EE_{CO}, FE_{CO}, cell voltage, stability and j_{CO} in this work with those of the state-of-the-art (c) NiNC electrodes,[31–33] and (d) Ag electrodes in a MEA.[34–39]

~15–20% higher j_{CO} at equal or lower cell voltage with higher energy efficiency towards CO. Although one Ag electrode reaches a higher j_{CO} (700 mA cm^{-2}), it does so with a lower FE_{CO} (85%) and EE_{CO} (32.5%). To further probe the catalytic performance of the MNC catalysts, we calculated the turnover frequencies (TOF) for the production of CO based on the total Ni content (derived from ICP-OES) (more details are provided in the Methods section) for the MNC catalysts listed in Table S1. It should be noted that not all Ni–N_x/C motifs contribute to catalytic activity for CO_2R, as a fraction of Ni species may exist within clusters/particles or remain inaccessible within the bulk structure. Furthermore, in MEA configurations, mass transport limitations are unavoidable to some extent, which can affect TOF analyses that typically assume negligible transport limitations. The NiNCNT-sim 800 °C catalyst indicated relatively higher apparent TOF (0.26 s^{-1}) at 3.2 V compared to the state-of-the-art NiNC catalysts tested at similar cell voltages, suggesting improved Ni-site utilization, which may originate from a more favorable catalyst layer morphology that facilitates CO_2 transport and alleviates local mass-transport limitations.

One of the key reasons for the high stability of the NiNCNT-sim 800 °C electrode (Fig. 2b) could potentially be due to the incorporation of polytetrafluoroethylene (PTFE) particles into the electrode structure, which has been shown to mitigate flooding of the electrode by modifying the hydrophobicity.[40] Flooding refers to the blockage of the GDL pores with liquid, hampering CO_2 transport.[41] Static contact angle measurements revealed a highly hydrophobic surface (144.35°) for the NiNCNT-sim 800 °C electrode (Fig. S1b). The stability test for the NiNCNT-sim 800 °C electrode eventually led to 16% FE towards H_2 after 230 hours of chronopotentiometry at 100 mA cm^{-2}. We then sought to further improve the stability of this electrode by operating the cell under pulsed conditions through alternating between chronopotentiometry at the target current density for 3 s followed by 0 mA cm^{-2} for 1 s. When utilizing a current density of 200 mA cm^{-2}, selected to study the stability of the electrode at more industrially relevant conditions, the NiNCNT-sim 800 °C electrode maintained the performance for 70 hours, showing only a 10% change in the cell voltage and a 11% decrease in FE_{CO}. For the stability test at a current density of 100 mA cm^{-2} under pulsed conditions, the MEA sustained continuous operation for 300 hours with just 11% and 17% changes in the cell voltage and FE_{CO}, respectively (Fig. S2a and b). Improved stability of the NiNCNT-sim 800 °C electrode under pulsed conditions compared to the continuous galvanostatic operation at 100 mA cm^{-2} as demonstrated in Fig. 2b (210 hours of stability) and Fig. S2b (300 hours of stability), can likely be associated with the regulation of catalyst microenvironment during the recovery periods of the pulsed technique. In the recovery periods (an applied current density of 0 mA cm^{-2} for 1 s), anions such as CO_3^{2-} formed because of the reaction between OH^- ions (produced in CO_2R and HER) with CO_2 gas, can diffuse away from the catalyst surface. This periodic adjustment helps to suppress salt precipitation, mitigating performance degradation.[42,43]

Although pulsed electrolysis utilizing a current density of 200 mA cm^{-2} enabled relatively stable performance of the NiNCNT-sim 800 °C electrode in a MEA over 70 hours; degradation ultimately emerged after ~70 hours as the FE towards H_2 increased to 12% with a cell voltage of 3.05 V compared to the starting point with FE_{H_2} of only 1% and cell voltage of 2.75 V (Fig. S2a). We then explored the possible contributions of the reversible performance losses that may originate from salt precipitation and/or flooding. After 70 hours of CO_2R, we rinsed the NiNCNT-sim 800 °C electrode to remove any possible salts that had formed, followed by drying the electrode to reverse the impacts of flooding. After re-assembly and applying the chronopotentiometry test at 200 mA cm^{-2}, the FE towards H_2 decreased to 8.2% (Fig. S3) from the 12% recorded after 70 hours of stability test.

The CO_2R performance of the CNT supported catalyst prepared *via* the simultaneous wetness impregnation method without the addition of nickel nitrate (NCNT-sim 800 °C) was also investigated and found to provide a maximum j_{CO} of only 20 mA cm^{-2} at a cell voltage of 2.7 V (Fig. S4a), highlighting the key role of Ni in creating catalytically active CO_2R sites, that are likely in the form of Ni–N_x as shown by previous literature.[20] It is postulated that the production of small amounts of CO in the Ni-free NCNT-sim 800 °C electrode likely arises from the residual transition metals (*e.g.*, Co and Fe) present in the structure of the CNT or trace metal impurities in the precursors used during catalyst synthesis, which upon pyrolysis can potentially form CoNC and FeNC active sites that are known to be catalytically active, an occurrence that was previously brought to light within the field of oxygen reduction electrocatalysis.[44,45] We also evaluated the impact of using glucose as a chelating agent during catalyst synthesis and observed a clear performance gain: at 3.2 V, the NiNCNT-sim 800 °C electrode delivered a j_{CO} of 558 mA cm^{-2} with FE_{CO} of 92%, outperforming the electrode prepared without glucose (NiNCNT-sim 800 °C w/o glucose) with a j_{CO} of 402 mA cm^{-2} and FE_{CO} of 89% (Fig. S4b and c).

We also probed the impact of catalyst synthesis on the CO_2R performance of the electrodes prepared using CB as the catalyst support. The NiNCB-sim 800 °C electrode demonstrated a j_{CO} of 154 mA cm^{-2} at 3.2 V and FE_{CO} of 75%, a significant improvement over the NiNCB-phys 800 °C electrode with a j_{CO} of 83 mA cm^{-2} and FE_{CO} of 55% at 3.2 V (Fig. S5a and b). As the porosity and CO_2 transport within the electrode can be tuned by engineering the catalyst support, we compared the CO_2R performance of the NiNCNT and NiNCB electrodes within an MEA. The NiNCNT electrodes provided significantly higher j_{total} and j_{CO} values across a broad cell voltage window (2.5–3.2 V) compared to the NiNCB electrodes (Fig. 1 and Fig. S5a–c). For example, the NiNCNT-sim 800 °C electrode demonstrated a j_{CO} of 558 mA cm^{-2} and FE_{CO} 92% at 3.2 V, outperforming the NiNCB-sim 800 °C electrode with a j_{CO} of 154 mA cm^{-2} and FE_{CO} of 75% at the same operating cell voltage as illustrated in Fig. 1b and Fig. S5a, respectively. In line with the NiNCNT electrodes, the NiNCB electrodes display the same pyrolysis-temperature-dependent performance, where

NiNCB-sim 800 °C (with j_{CO} of 154 mA cm^{-2} at 3.2 V) surpasses NiNCB-sim 900 °C (j_{CO} of 99 mA cm^{-2} at 3.2 V) (Fig. S5a and c).

Catalyst characterization

The Brunauer–Emmett–Teller (BET) surface area and pore volume were evaluated for acid-treated CNT, CB, NiNCNT-sim, NiNCNT-phys, NiNCB-sim, and NiNCB-phys catalysts synthesized at pyrolysis temperatures ranging from 700 to 900 °C (Fig. 6a–f and Table S2). The N_2 adsorption–desorption isotherm of the acid-treated CNT shown in Fig. S6f corresponds to a type IV isotherm, while acid-treated CB exhibits a combined type I + IV isotherm, indicating the presence of both microporous and mesoporous structures.[46] The NiNCNT-sim 800 °C catalyst demonstrated higher specific surface area (596 m^2 g^{-1}) compared to the acid-treated CNT (486 m^2 g^{-1}). This can be correlated to the presence of Ni during catalyst synthesis, which likely promotes microporosity development by catalyzing carbonization of the glucose/melamine during pyrolysis.[47] By increasing the pyrolysis temperature to 900 °C, the specific surface area slightly decreased for the NiNCNT-sim 900 °C catalyst (422 m^2 g^{-1}) compared to the NiNCNT-sim 800 °C catalyst (596 m^2 g^{-1}) as shown in Table S2. On the other hand, the catalyst prepared using the physical mixing method (NiNCNT-phys 800 °C) demonstrated a lower specific surface area (373 m^2 g^{-1}) compared to the acid-treated CNT (486 m^2 g^{-1}). This suggests that the inhomogeneous dispersion of melamine may have partially blocked inter-CNT spaces, reducing the specific surface area.

To probe how the carbon support and synthesis route impact the physical properties of the NiNC catalyst, we also analyzed the BET surface areas of the NiNCB catalysts. NiNCB-sim 800 °C showed a markedly higher specific surface area (1019 m^2 g^{-1}) than both the acid-treated CB (758 m^2 g^{-1}) and NiNCB-phys 800 °C catalyst (645 m^2 g^{-1}), highlighting that the simultaneous wetness impregnation method promotes additional porosity development in the catalyst structure during pyrolysis. The enhanced surface area of the NiNCB-sim 800 °C and NiNCNT-sim 800 °C catalysts (Table S2) compared to the NiNCB-phys 800 °C and NiNCNT-phys 800 °C counterparts correlates well with their higher CO_2R activity and selectivity (Fig. S5a, b and Fig. 1b, e). Higher specific surface area can expose more electrochemically active sites and enhance the porosity of the catalyst that can facilitate CO_2 transport. The impact of glucose on the physical characteristics of the NiNC catalyst was also supported by BET data. Improved CO_2R performance observed for the NiNCNT-sim 800 °C electrode (Fig. 1b) compared to the NiNCNT-sim 800 °C w/o glucose electrode (Fig. S4b) can also be attributed to the formation of abundant micropores (<2 nm) originated from glucose carbonization during pyrolysis, as evidenced by pore-size distribution analysis and micropore surface area in the NiNCNT-sim 800 °C catalyst (Fig. S6b and Table S2).

High-resolution TEM (HRTEM) images (Fig. 3a and b) reveal that the NiNCNT-sim 800 °C structure is covered with a partially amorphous and partially crystalline surface layer, which is absent in the structure of the pristine CNT as shown in Fig. 3c. This overlayer is a typical feature of the pyrolyzed carbonaceous materials such as glucose.[19] To further evaluate the characteristics of this overlayer; we compared the diffraction patterns of this layer in the NiNC catalysts with the pristine carbon supports (CB and CNT). Fast Fourier transform (FFT) patterns for the NiNCNT-sim 800 °C (Fig. 3a and b) and NiNCB-sim 800 °C (Fig. S7a) show diffuse rings, supporting the presence of an isotropic carbon overlayer derived from partial carbonization of glucose/melamine during pyrolysis, whereas acid-treated CNT (Fig. 3c) and CB (Fig. S7b) demonstrate arc-like orientation, which is characteristic of the well-ordered sp^2 carbon (002). *Z*-Contrast high-angle annular dark-field and aberration-corrected scanning transmission electron microscopy (HAADF-STEM) images exhibited isolated bright spots on the CNT (Fig. 3d–f), which are suggested to be Ni based on the Ni L-edge signal obtained by the electron energy loss spectroscopy (EELS, Fig. 3g and h). The presumably atomically dispersed Ni sites are also anchored on the carbon layer derived from the glucose/melamine carbonization as well as on the sidewalls of CNT (Fig. 3d). STEM-EDX (energy dispersive X-ray spectroscopy) elemental mapping further shows the distribution of Ni and N throughout the carbon support for NiNCNT-sim 800 °C (Fig. 3i) and NiNCB-sim 800 °C (Fig. S7e) catalysts.

To further analyze the impact of synthesis method, chelating agent, and carbon support on the structure of the synthesized NiNC catalysts, we used Raman spectroscopy. Raman spectra show the D and G band peaks for all catalysts located at ~1350 cm^{-1} and 1590 cm^{-1}, respectively (Fig. S8a and b). NiNCNT-sim 800 °C catalyst shows a lower I_D/I_G ratio and a clear 2D band at ~2700 cm^{-1} compared to the NiNCNT-phys 800 °C catalyst. We observed the same trend for the catalysts prepared using CB support as the NiNCB-sim 800 °C catalyst demonstrated a lower I_D/I_G ratio compared to the NiNCB-phys 800 °C catalyst (Fig. S8b). NiNCNT-sim 800 °C w/o glucose shows a higher I_D/I_G indicating that glucose promotes graphitization of the carbon; FFT patterns further corroborate the partially graphitized nature of the glucose/melamine-derived carbon overlayer as shown in Fig. 3b. The X-ray diffraction (XRD) also displays two broad peaks associated with the (002) and (101) planes of the graphitic carbon with no metallic Ni peaks observed for any of the NiNC catalysts, likely due to the acid washing step implemented during the catalyst synthesis (Fig. S8c).

X-ray photoelectron spectroscopy (XPS) was also performed to assess the effects of synthesis method, carbon support, and pyrolysis temperature on the concentration and identity of the resulting N functionalities. Elemental quantification results derived from XPS, shown in Table S3, reveal slightly higher Ni atomic percentages for the NiNCNT-sim 800 °C catalyst (0.53%) compared to the NiNCNT-phys 800 °C catalyst (0.42%). Considering the near-surface sensitivity of XPS, inductively coupled plasma optical emission spectroscopy (ICP-OES) was performed to determine the bulk Ni content in the synthesized catalysts (Table S3). The NiNCNT-sim 900 °C catalyst exhibits the highest Ni loading, which can be attributed to the formation of carbon-encapsulated Ni clusters *via* metal-catalyzed graphitization at elevated temperatures. These encapsulated Ni species are

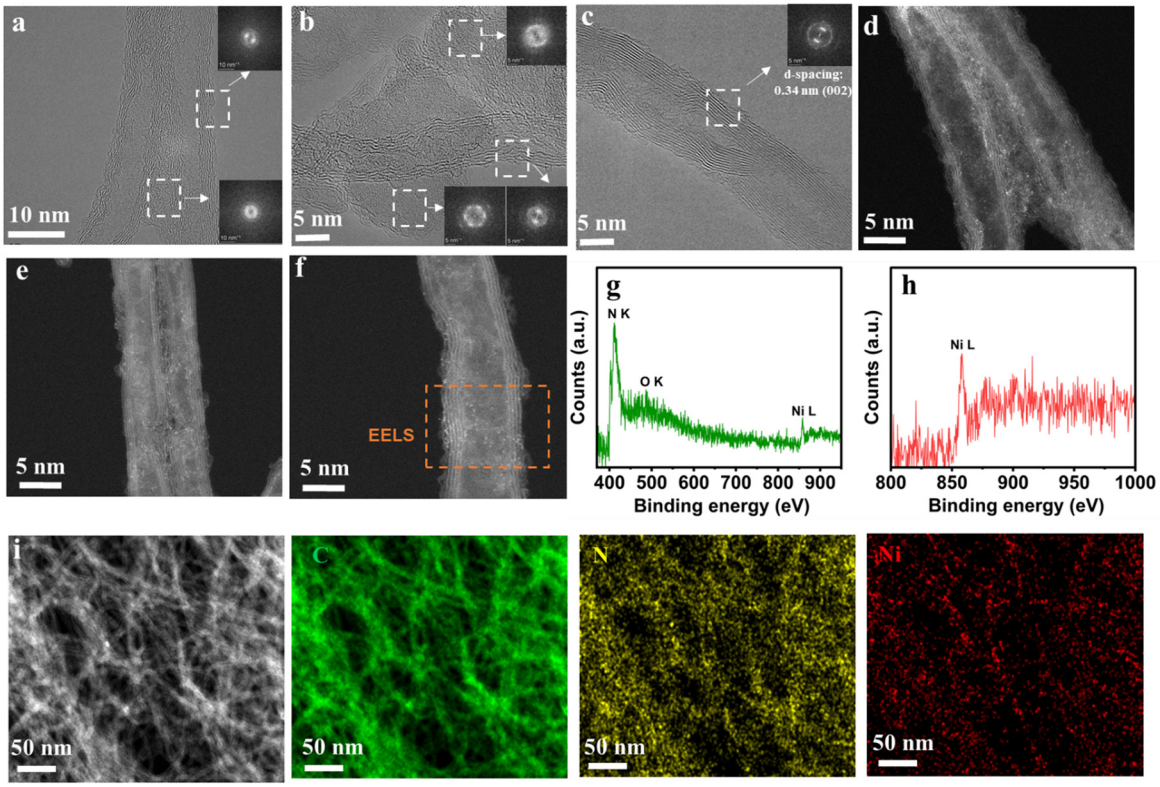

Fig. 3 Morphological and compositional analysis of NiNCNT-sim 800 °C catalyst. (a) and (b) HRTEM image of NiNCNT-sim 800 °C (c) HRTEM image of acid-treated CNT (d)–(f) HAADF-STEM images of NiNCNT-sim 800 °C catalyst (g) and (h) EELS spectra of NiNCNT-sim 800 °C catalyst, and (i) EDX maps of NiNCNT-sim 800 °C catalyst.

possibly protected by graphitic carbon layers and might not have been effectively removed during the acid leaching process. The CB-based catalyst (NiNCB-phys 800 °C) showed a significantly lower near-surface Ni content (0.1 at%) compared to CNT-based catalysts. This discrepancy suggests that a substantial fraction of Ni active sites might be embedded within the aggregated carbon black particles, rendering them inaccessible to near-surface sensitive techniques such as XPS. The high-resolution N 1s spectra (Fig. 4a–d) were deconvoluted into pyridinic N (~398.5 eV), Ni–N (~399.2 eV), pyrrolic N (~400.2 eV), graphitic N (~401.8 eV), and oxidized N (~406.7 eV).[25] As depicted in Fig. 4e, both the proportion of N atoms residing in pyridinic form and the total atomic percentage of N in the catalyst were reduced by increasing pyrolysis temperature from 700 to 900 °C for NiNCNT-sim catalysts. We also estimated the fraction of near-surface Ni present as Ni–N_x species in NiNCNT-sim 800 °C and NiNCNT-phys 800 °C catalysts (by multiplying the Ni atomic percentage by the relative abundance of Ni–N_x contributions obtained from XPS analysis (Table S3)). This value is significantly higher for NiNCNT-sim 800 °C (0.29) compared to NiNCNT-phys 800 °C (0.06), indicating enhanced formation of Ni–N_x sites using the simultaneous wetness impregnation method. While this parameter cannot be directly correlated with CO_2R performance due to mass transport limitations, since it assumes that all surface Ni–N_x sites are accessible to CO_2, it nevertheless provides useful insight into the density of Ni–N_x sites in the NiNCNT catalysts.

To further elucidate the role of glucose during catalyst synthesis in terms of maintaining Ni in atomically dispersed form to produce Ni–N_x sites, the N 1s peak deconvolution of NiNCNT-sim 800 °C w/o glucose was performed. NiNCNT-sim 800 °C w/o glucose showed a lower proportion of N atoms residing in the Ni–N form (10.54%), as well as a lower total atomic percentage of N (0.96%) compared to the NiNCNT-sim 800 °C catalyst with total atomic percentage of N of 1.21% and 24.97% proportion of N atoms residing in the Ni–N form as shown in Table S3 and Fig. 4d. Both catalysts were synthesized with the same nominal Ni loading (0.69 wt% of the total precursor mixture including CNT, glucose and melamine). This suggests the formation of small Ni clusters in the absence of glucose during pyrolysis. Any Ni clusters that were formed probably have been leached out during the acid washing step (Scheme 1), thereby resulting in the reduced final Ni concentration in the glucose-free sample. Consistent with previous reports,[48,49] lower N contents in the catalysts with the increase of pyrolysis temperature do not correspond to a decline in CO_2R performance of the NiNC electrodes (Fig. 1). On the other hand, the proportion of N atoms residing in the Ni–N form illustrates an upward trend by increasing pyrolysis temperature. This suggests that the catalytic activity in CO_2R is governed primarily by the specific chemical nature and local

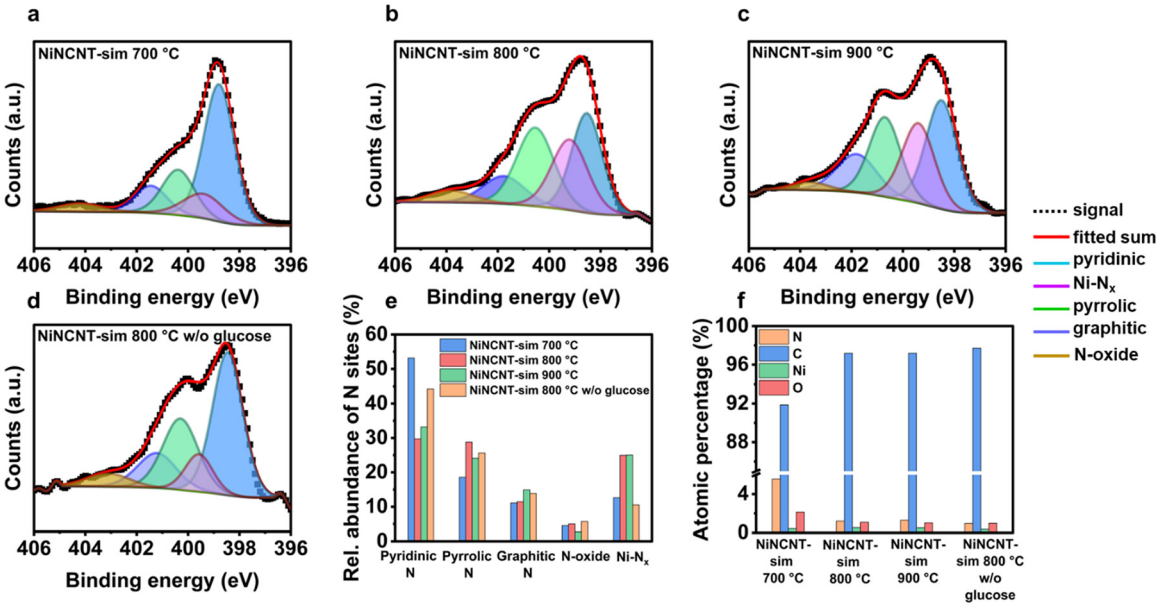

Fig. 4 Deconvoluted high resolution N 1s XPS spectra of (a) NiNCNT-sim 700 °C, (b) NiNCNT-sim 800 °C (c) NiNCNT-sim 900 °C, (d) NiNCNT-sim 800 °C w/o glucose, (e) relative abundance of different N sites in the NiNCNT catalysts, and (f) atomic percentages of N, C, Ni, and O in the synthesized NiNCNT-sim catalysts.

environment of the nitrogen functional groups, rather than their overall abundance.

The local coordination environment of Ni atoms in the prepared catalysts was analyzed using X-ray absorption near-edge structure (XANES) and extended X-ray absorption fine structure (EXAFS) analyses. The XANES spectrum of NiPc as a reference demonstrates a weak pre-edge feature at position A and a strong absorption peak at position B (Fig. 5a). The former arises from a local electric quadrupole transition (1s → 3d), while the latter corresponds to the dipole-allowed transition (1s → 4p$_z$) characteristic of Ni–N$_4$ centers.[50] The main edge position of the NiNCNT-sim, NiNCNT-phys, NiNCB-sim, and NiNCB-phys catalysts synthesized at different pyrolysis temperatures is slightly higher than the Ni foil and lower than NiO (Fig. 5a, b and Fig. S9); highlighting that the oxidation state of Ni is between 0 and +2, which is characteristic of atomically dispersed NiNC catalysts.[19]

Fourier transform (FT) k^2-weighted EXAFS spectra of the synthesized catalysts were studied in R space (Fig. 5c–f). As shown in Fig. 5e (a magnified view of Fig. 5c), the dominant peak in the Ni K-edge EXAFS-FT spectra of the NiNCNT-sim 700 °C and NiNCNT-sim 800 °C catalysts appears at approximately 1.45 Å (non-phase-shift-corrected), which is attributed to the Ni–N scattering path within the Ni–N$_4$ coordination. The major peak in the EXAFS-FT spectra of NiNCNT-sim 900 °C, on the other hand, was observed at 1.38 Å, highlighting that the average Ni–N radial distance might be shorter than that of the NiPc (~1.45 Å), demonstrating different Ni–N coordination in NiNCNT-sim 900 °C compared to NiPc, and the NiNCNT catalysts pyrolyzed at 700 and 800 °C. This was further supported by EXAFS fitting, which demonstrates that the Ni–N coordination in NiNCNT-sim 700 °C, NiNCNT-sim 800 °C, and NiNCNT-sim 900 °C is 4.08, 4.12, and 3.32, respectively (Table S4 and Fig. S10). A similar trend was also reported by Wang *et al.*,[22] showing that increasing pyrolysis temperature from 800 to 900 °C for MNC catalysts (M = Fe, Ni, Co, Cu, and Mn) led to a shorter M–N radial distance. In addition to the primary Ni–N scattering peak, the EXAFS-FT spectrum of the NiNCNT-sim 800 °C w/o glucose catalyst exhibits a shoulder near ~2.2 Å (Fig. 5d), likely arising from Ni–Ni scattering associated with the presence of Ni clusters in the catalyst synthesized without glucose. Notably, such short-range Ni–Ni order can be invisible by XRD as shown in Fig. S8c, highlighting the key role of EXAFS in evaluating the local structure of the synthesized catalysts. This is also in line with the HER activity of the NiNCNT-sim 800 °C w/o glucose electrode (Fig. S4b), which can be correlated to the presence of small Ni clusters.[51]

We also analyzed the local chemical structure of the catalysts prepared using CB support. NiNCB-sim 800 °C, NiNCB-sim 900 °C, and NiNCB-phys 800 °C catalysts display a main peak at about 1.41 Å corresponding to the first-shell Ni–N coordination (Fig. 5f). The similar peak position to that of the NiPc suggests that the Ni centers in NiNCB catalysts are primarily coordinated in the form of Ni–N$_4$ geometry (Table S4). For NiNCB-phys 800 °C catalyst, an additional peak at 2.2 Å was also found in the FT-EXAFS spectrum (Fig. 5f), depicting the existence of small Ni clusters.[22] This likely arises from the non-uniform distribution of melamine, which limits the availability of N coordination sites and promotes Ni clustering. This is also consistent with the CO_2R performance results showing a higher HER selectivity for the NiNCB-phys 800 °C catalyst compared to the NiNCB-sim 800 °C catalyst (Fig. S5a and b). The wavelet transformed (WT) plots of the reference samples (NiO, NiPc, and Ni foil) and NiNCNT-sim 800 °C catalyst are also presented

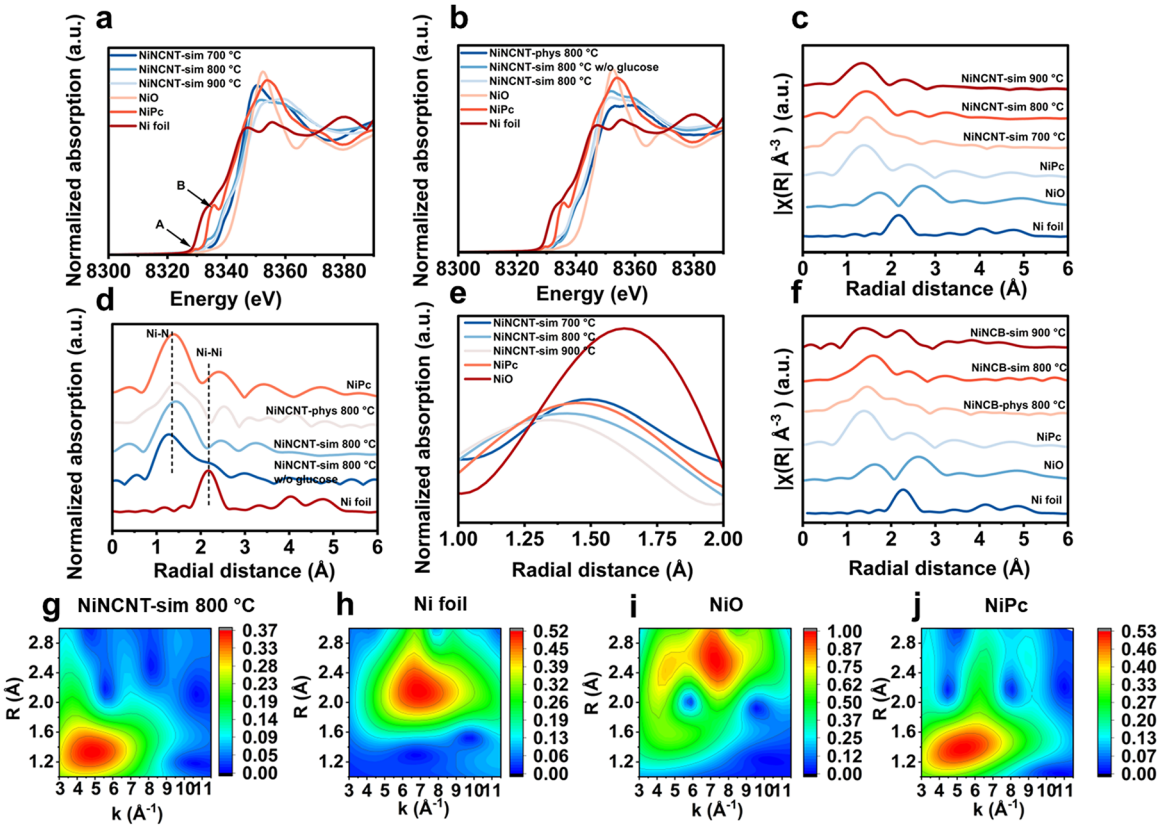

Fig. 5 Chemical states and atomic coordination environment analysis of synthesized catalysts. XANES spectra of the (a) and (b) NiNCNT catalysts synthesized at different pyrolysis temperatures, melamine impregnation method, and without glucose, (c)–(f) FT-EXAFS spectra at the Ni K-edge of NiNC catalysts synthesized at different pyrolysis temperatures, melamine impregnation method, without glucose, and different carbon substrates, wavelet transforms (WT) of (g) NiNCNT-sim 800 °C, (h) Ni foil, (i) NiO, and (j) NiPc.

in Fig. 5g–j. The NiNCNT-sim 800 °C catalyst shows a maximum lobe at 5.8 $Å^{-1}$, corresponding to the Ni–N bonding when compared to NiPc. No intensity maximum of Ni–Ni bonding is detected for the NiNCNT-sim 800 °C catalyst at higher wave numbers.

In situ electrochemical impedance spectroscopy (EIS) was employed to study the charge transfer, electrolyte resistance, and mass transport in the prepared electrodes. Distribution of the relaxation times (DRT) analysis was conducted by deconvoluting the impedance data to correlate the electrochemical reactions with their corresponding relaxation times.[52] As the applied cell voltage increases, the charge transfer resistance (R_{ct}) decreases for the NiNCNT-sim 800 °C (Fig. S11a), NiNCNT-sim 800 °C w/o glucose (Fig. S11b), NiNCNT-phys 800 °C (Fig. S11c), NiNCB-phys 800 °C (Fig. S12a), and NiNCB-sim 800 °C (Fig. S12b) electrodes. The correlated DRT plots show 3 distinguished peaks as demonstrated in Fig. S11d–f. The P_1 peak located at approximately 2.0×10^{-6} s shows an inconspicuous variation with the cell voltage, suggesting the polarization represented by this peak might be irrelevant to R_{ct} of CO_2R, and it can be more correlated with the contact resistance. The P_2 peak ($\sim 2.0 \times 10^{-5}$ s), on the other hand, gradually diminishes with increasing cell voltage (Fig. S11d), whereas j_{CO} rises sharply by increasing the cell voltage from 2.5 to 3.2 V (Fig. 1b). This opposing trend suggests P_2 is unlikely to reflect R_{ct} of CO_2R and is more consistent with a process associated with the HER. The peak at about 1.0×10^{-3} s (P_3) can be attributed to the CO_2 charge transfer in the NiNCNT-sim 800 °C electrode (Fig. S11d). To further elucidate the origin of the polarization associated with the P_3 peak in the DRT spectra, we performed complementary CO_2R performance testing (Fig. S13a and b) and DRT analyses (Fig. S13c–f) under a diluted feed (CO_2/Ar = 1 : 1) using the NiNCNT-sim 800 °C electrode in a MEA. The P_3 peak ($\tau \approx 10^{-3}$ s) gradually decreases with increasing cell voltage in both pure CO_2 and CO_2/Ar atmospheres (Fig. S13d and f). Considering the concurrent increase in FE towards H_2 with increasing cell voltages under CO_2/Ar (Fig. S13b), we speculate that this peak reflects contributions from polarization represented by both CO_2R and the competing HER.

To further evaluate the impact of glucose, we studied the electrochemical behaviour of NiNCNT-sim 800 °C w/o glucose electrode. At 3.2 V, selected as a reference condition where mass transfer limitations are more likely to arise, the resistance value of P_3 in the NiNCNT-sim 800 °C w/o glucose electrode is slightly higher than the NiNCNT-sim 800 °C electrode, suggesting higher charge transfer resistance for the electrode prepared without glucose (Fig. S11e). We also investigated the role of the

catalyst synthesis method on the electrochemical behaviour of the synthesized NiNC electrodes. NiNCNT-phys 800 °C electrode indicated higher charge transfer resistances compared to the NiNCNT-sim 800 °C electrode at different cell voltages (Fig. S11a and c), which are also in line with the DRT results. P_3 peak shifted to lower relaxation times and amplitude of the impedance, indicating improved CO_2R kinetics for NiNCNT-sim 800 °C compared to the NiNCNT-phys 800 °C electrode (Fig. S11f). Similarly, NiNCB-sim 800 °C electrode depicted moderately lower R_{ct} at higher cell voltages compared to NiNCB-phys 800 °C electrode as demonstrated in Fig. S12a and b. These highlight improved interfacial kinetics in the NiNCB-sim 800 °C electrode, which is correlated with the better electronic coupling between Ni–N_x sites and the carbon backbone, fewer resistive contact points within the catalyst layer, and/or a more favorable local reaction environment (wettability/ion transport) at the most active domains. Possible inhomogeneous dispersion of the Ni–N_x sites derived from the physical mixing of the N precursor in the catalyst synthesis could also potentially increase the interfacial charge transfer resistance. We then sought to investigate the impact of catalyst support on the interfacial charge transfer/charge transfer resistance of the NiNC electrodes. Based on the DRT results at 3.2 V as illustrated in Fig. S12c, the polarization resistance value of P_3 decreased for the NiNCNT-sim 800 °C electrode compared to the NiNCB-sim 800 °C electrode, indicating improved charge transfer for the NiNCNT-sim 800 °C electrode.

To analyze the effective interfacial area of the catalyst layer wetted by electrolyte, we used cyclic voltammetry (CV) measurements to calculate the double-layer capacitance (C_{dl}). The NiNCNT-sim 800 °C electrode indicated higher C_{dl} (6.59 mF cm^{-2}) compared to NiNCNT-sim 800 °C w/o glucose (4.40 mF cm^{-2}) catalyst as illustrated in Fig. S14a, b and S15, respectively. We noted two chief reasons why the NiNCNT-sim 800 °C electrode shows higher double layer capacitance compared to the NiNCNT-sim 800 °C w/o glucose electrode: (1) formation of the carbon layer derived from glucose carbonization (supported by BET results (Table S2) and HRTEM images (Fig. 3b)), which creates additional micropores and increases the electrochemically exposed surface area; and (2) impact of glucose on isolating Ni sites during pyrolysis, which might be attributed to a chelation-assisted stabilization mechanism, in which hydrated Ni ions can interact with hydroxyl groups of the α-D-glucose molecule, as illustrated in Scheme 1. The possible chelation effect of glucose can also be indirectly supported through EXAFS of the resulting catalyst. The control sample (NiNCNT-sim 800 °C w/o glucose) prepared in parallel, except for no addition of glucose, exhibits a shoulder near ~2.2 Å in the EXAFS spectra (Fig. 5d), arising from Ni–Ni scattering; in addition to the primary Ni–N scattering peak observed near ~1.45 Å. The absence of the Ni–Ni scattering peak at 2.2 Å in the NiNCNT-sim 800 °C catalyst is associated with the presence of glucose during synthesis, likely due to the chelating role that glucose plays in suppressing the agglomeration of Ni during pyrolysis. On the other hand, BET results (Table S2) indicate that glucose modifies the local textural environment during synthesis, resulting in a slightly higher micropore and mesopore surface area in the NiNCNT-sim 800 °C catalyst compared to the control sample synthesized without glucose (NiNCNT-sim 800 °C w/o glucose). Such changes in pore structure can be related to interactions between glucose-derived hydroxyl functional groups and hydrated Ni species, which could impact the precursor dispersion and carbonization pathways, developing a different porous structure after pyrolysis. A similar chelation effect has been previously reported for the FeNC atomically dispersed catalyst for oxygen reduction reaction (ORR).[19]

Notably, the NiNCNT-phys 800 °C electrode showed lower C_{dl} (3.40 mF cm^{-2}) compared to the NiNCNT-sim 800 °C electrode (6.59 mF cm^{-2}) (Fig. S15), underscoring the beneficial effect of simultaneous wetness impregnation of melamine during synthesis on the electrolyte–electrode interactions and a potentially increased density of Ni–N_x sites enabled by the simultaneous wetness impregnation method. This trend is consistent with the lower BET surface area of the NiNCNT-phys 800 °C catalyst (373 m^2 g^{-1}) relative to the NiNCNT-sim 800 °C (596 m^2 g^{-1}) catalyst, suggesting restricted pore accessibility arising from non-uniform melamine dispersion during the physically mixed method, which leads to Ni agglomerates remaining in the structure of the catalyst even after acid washing (Scheme 1). The NiNCNT-sim 800 °C electrode also exhibits a higher double-layer capacitance (6.59 mF cm^{-2}) compared to NiNCB-sim 800 °C (4.40 mF cm^{-2}) (Fig. S15). This difference can be attributed to the higher content of mesopores in the NiNCNT-sim 800 °C catalyst, whereby mesopores have been shown to enhance electrolyte accessibility, increasing the electrochemically accessible surface area.[53]

We also characterized the NiNCNT-sim 800 °C electrode after stability testing at 200 mA cm^{-2} under pulsed conditions (3 s at 200 mA cm^{-2} and 1 s at 0 mA cm^{-2}) for 70 hours to evaluate the contribution of the irreversible catalyst degradation on performance loss. To do so, we performed post-catalysis TEM and XAS characterization on the NiNCNT-sim 800 °C electrode after stability testing. High resolution HAADF-STEM images indicate isolated bright spots (Fig. S16a and b), which are suggested to be Ni based on the EDX elemental mapping results (Fig. S16c). On the other hand, Fig. S17 shows HAADF-STEM images taken from a different region of the NiNCNT-sim 800 °C catalyst after stability testing that shows the formation of some Ni nanoparticles. Consistent with this, the Fourier-transformed k^2-weighted EXAFS spectrum exhibits the main peak around 1.45 Å which is attributed to the Ni–N scattering path within the Ni–N_4 coordination. Moreover, the EXAFS spectra show a peak at ~2.2 Å (Fig. S18a), corresponding to Ni–Ni scattering, which indicates partial aggregation of Ni to form Ni-based particles or clusters during stability testing. Linear combination fitting (LCF) analysis was used to quantify the proportion of Ni atoms within the catalyst that exist as metallic Ni, Ni-oxide or atomically dispersed Ni–N_x species (more details are provided in the Methods section). This analysis revealed a decrease in the proportion of Ni atoms that exist as Ni–N_x species in the catalyst, going from 87% of the Ni atoms in the pristine catalyst to 65% of the Ni atoms in the

catalyst after stability testing (Fig. S18b). By extension, a higher proportion of Ni atoms in the catalyst after stability testing existed as metallic Ni or Ni-oxide species. These results along with the CO_2R performance results of the NiNCNT-sim 800 °C electrode after stability testing at 200 mA cm^{-2} for 70 hours (after rinsing to remove any possible salts) (Fig. S3) indicate that a fraction of the performance loss can also be attributed to irreversible catalyst deactivation associated with the formation of Ni nanoparticles.

Tomographic analysis

To evaluate the impact of catalyst support and interparticle porosity on the CO_2R performance of the NiNCNT-sim 800 °C and NiNCB-sim 800 °C electrodes in MEA, we employed FIB-SEM tomography imaging to identify the morphology of the catalyst layer, which was then coupled with COMSOL Multiphysics to evaluate the morphological impacts on the CO_2 transport (Fig. 6a, Note S1, and Fig. S19). Three sub-volumes ($250 \times 250 \times 250$ nm^3) were randomly selected from distinct regions of each sample and simulated independently. This approach enables us to account for heterogeneity of the catalyst layers while remaining within feasible computational limits. Each sub-volume was decomposed into two complementary computational domains: the pore (gas) phase, which governs gas flow (Stokes equations) and gas diffusion (Fick's law), and the solid phase (catalyst structure), which resolves electronic transport *via* Ohm's law (Table S5). Effective diffusivity, permeability, and effective conductivity were averaged over three sub-volumes (Table S6). The simulations were performed under steady-state conditions, assuming single-phase gas transport within the pore space. As such, dynamic multiphase phenomena that can arise during electrolysis such as electrolyte flooding, salt precipitation, and carbonate formation within the catalyst layer, are not explicitly captured in the present model.

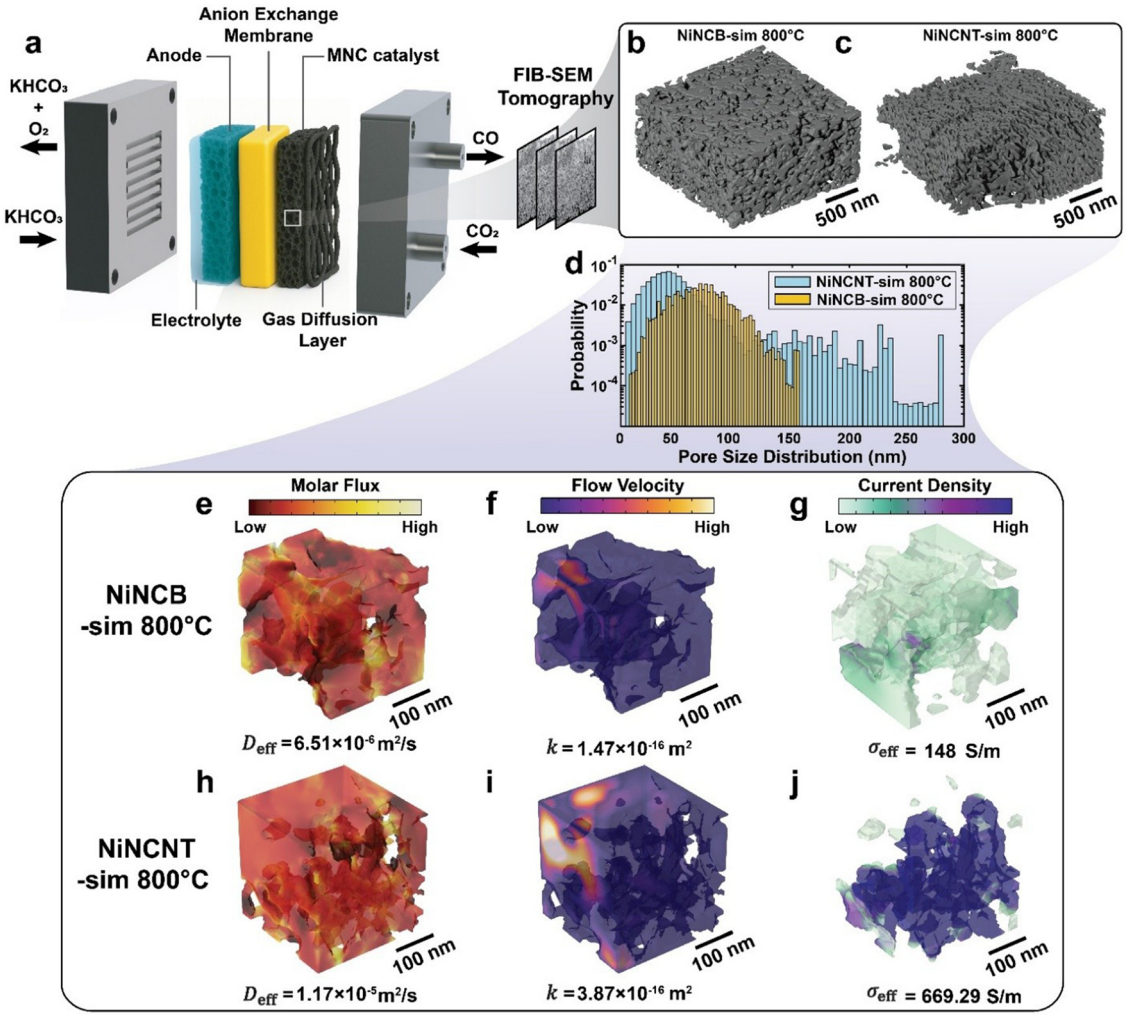

Fig. 6 (a) Schematic of the MEA electrolyzer system, 3D FIB-SEM reconstructions of $1 \times 2 \times 2$ μm^3 volumes for (b) NiNCB-sim 800 °C, (c) NiNCNT-sim 800 °C catalyst layers, (d) pore size histogram for, NiNCB-sim 800 °C and, NiNCNT-sim 800 °C based catalyst layers, COMSOL Multiphysics simulation results on $250 \times 250 \times 250$ nm^3 sub-volumes for (e) CO_2 molar-flux distributions within the pores for NiNCB-sim 800 °C, (h) NiNCNT-sim 800 °C catalyst layers, (f) simulation results for flow fields in NiNCB-sim 800 °C, (i) NiNCNT-sim 800 °C samples, (g) current density distribution results within the catalyst particles for NiNCB-sim 800 °C, (j) NiNCNT-sim 800 °C catalyst layer. Color scales in all panels are normalized to their respective maximum.

3D reconstructions from FIB-SEM tomography (Fig. 6b and c) show that the NiNCNT-sim 800 °C catalyst particles are anisotropic and fibrous, whereas the NiNCB-sim 800 °C catalyst particles are isotropic and tortuous. Quantitative pore analysis demonstrates that the NiNCNT-sim 800 °C catalyst layer attains a porosity of 34%, exceeding the 31% recorded for the NiNCB-sim 800 °C. Moreover, NiNCNT-sim 800 °C catalyst layer exhibits a hierarchical pore network with a broad pore size distribution ranging from 2 to 278 nm, while the NiNCB-sim 800 °C is confined to a narrower pore size ranging from 2 to 154 nm (Fig. 6d).

The observed differences in 3D geometry and pore size translate directly to the simulated CO_2 molar-flux maps (Fig. 6e and h): NiNCNT-sim 800 °C catalyst layer shows an effective CO_2 diffusivity of 1.17×10^{-5} m^2 s^{-1}. In contrast, the NiNCB-sim 800 °C electrode exhibits significantly lower diffusivity of 6.51×10^{-6} m^2 s^{-1}, underscoring possible structural bottlenecks and mass-transport limitations. The reconstructed CO_2 velocity fields (Fig. 6f and i), obtained by solving the Navier–Stokes equation for steady-state, laminar, incompressible flow, reveal pronounced differences in the CO_2 transport behavior within the two catalyst layers. The NiNCNT-sim 800 °C catalyst layer exhibits continuous flow pathways, indicative of higher local permeability and reduced viscous resistance. On the other hand, the NiNCB-sim 800 °C layer leads to localized stagnation zones with severely restricted fluid penetration (Fig. 6f). Moreover, the CO_2 permeability in the NiNCB-sim 800 °C is lower (1.47×10^{-16} m^2) than the NiNCNT-sim 800 °C catalyst layer (3.87×10^{-16} m^2). Higher CO_2 permeability shortens gas transport pathways and enables higher CO_2 concentration in the vicinity of active sites, contributing to improved CO selectivity as supported by CO_2R performance of the NiNCNT-sim 800 °C in MEA (Fig. 1b). Our simulation results also revealed that the effective electronic conductivity is significantly higher in the NiNCNT-sim 800 °C (669.29 S m^{-1}) compared to the NiNCB-sim 800 °C (148.00 S m^{-1}) catalyst layer (Fig. 6g and j).

To further understand how the architecture of the catalyst layer governs CO_2 transport and flooding/salt dynamics, we analyzed the stability of the NiNCB-sim 800 °C electrode in a MEA under pulsed chronopotentiometry, alternating the current density between 200 mA cm^{-2} for 3 s and 0 mA cm^{-2} for 1 s. Cell voltage increased by 14% from the initial value of 2.89 V, while FE towards CO dropped to 78% from the starting value of 98% within only 7 hours of electrolysis, as illustrated in Fig. S20. On the other hand, the NiNCNT-sim 800 °C electrode maintained the performance for 70 hours, showing only a 10% change in cell voltage and a 11% decrease in FE towards CO (Fig. S2a). Our steady-state simulation results depict that the NiNCNT-sim 800 °C catalyst layer exhibits enhanced mass transport, continuous flow, and more uniform current distribution, highlighting the key role of larger interparticle porosity in the catalyst layer. In contrast, NiNCB-sim 800 °C catalyst layer suffers from structural bottlenecks, restricted CO_2 flux, and highly localized current densities, which might accelerate degradation *via* salt precipitation and flooding.[54,55]

We further validated the modeling results by correlating intrinsic structural and transport properties such as permeability, effective diffusivity, and electronic conductivity with CO_2R performance in MEA. Given the inherent challenges in accurately determining limiting current density in porous MEA electrodes, two approaches were employed: a Fickian diffusion model assuming single-phase transport with constant properties, and a correlational analysis based on CO_2 effective diffusivity and permeability (see Note S2 and Fig. S21). The results show that the CNT-based catalyst layer enhances both diffusive transport (Table S7) and convective CO_2 penetration into the porous structure. This combined transport enhancement is directly reflected in CO_2R performance: while the NiNCB-sim 800 °C electrode reaches a plateau in partial current density towards CO at ~200 mA cm^{-2}, the NiNCNT-sim 800 °C electrode exhibits no such limitation within the studied range, achieving up to ~550 mA cm^{-2} (Fig. S22).

We also estimated the total Ni–N_x site density (sites g^{-1}) for the NiNCNT-sim 800 °C and NiNCB-sim 800 °C catalysts based on the Ni loading determined by ICP-OES with the fraction of Ni–N_x species obtained from linear combination fitting (LCF) of the XANES spectra (more details are provided in the Methods section). Both catalysts exhibit comparable total site densities (5.89×10^{22} and 4.95×10^{22} sites g^{-1} for NiNCNT-sim 800 °C and for NiNCB-sim 800 °C, respectively); however, NiNCNT-sim 800 °C demonstrates a significantly higher TOF than NiNCB-sim 800 °C, particularly at cell voltages >3 V, where mass transport limitations become more pronounced (Fig. S23). This suggests that, despite a similar density of Ni–N_x sites, only a fraction of these sites is accessible to CO_2R in the NiNCB-sim 800 °C catalyst compared to the NiNCNT-sim 800 °C catalyst. These findings are consistent with our FIB-SEM-based simulations, highlighting the key role of catalyst layer morphology and interparticle spacing in governing CO_2R performance in MEA systems.

Catalyst cost estimation

Despite the notion that MNC catalysts provide cost advantages over Ag catalysts for CO_2R to CO, there does not exist a detailed cost analysis to provide quantitative justification for these claims. Given the complexity and uncertainty surrounding the commercial scalability of MNC catalysts, it is essential to evaluate their production costs at early stages. Similar to more established electrochemical technologies such as fuel cells, catalyst cost can represent a significant fraction of the total system cost in CO_2 electrolyzers, especially in low volume production scales.[56] To this end, we estimated the cost of the NiNCNT-sim 800 °C catalyst developed in this work through the simultaneous wetness impregnation method (Scheme 1). More details on the cost estimation method are provided in the SI (Note S3 and Fig. S24–S27). According to the CatCost[57] tool applied in this study, the projected cost of the NiNCNT-sim 800 °C catalyst based on the CapEx/OpEx method is substantially lower ($589.68 USD per kg) compared to that of the Ag-based cathode materials (~$1900 USD per kg) reported in the literature for CO_2R electrolyzers.[58]

A Sankey diagram (Fig. S28) shows that the NiNCNT-sim 800 °C projected purchase cost is dominated by the cost of carbon support and operating costs of the catalyst synthesis, highlighting a clear opportunity for cost reduction through using lower-cost carbon supports, and reducing the operating costs of the catalyst synthesis through process intensification. As an example, incorporating low-cost carbon supports with engineered pore structures, such as biomass-derived carbons (*e.g.*, biochar) may offer viable pathways to reduce the catalyst cost.[62] In parallel, engineering the support morphology to achieve higher interparticle porosity, as supported by our FIB-SEM/Multiphysics results, can enhance the CO_2R performance. Sensitivity analysis also depicts the effect of different input parameters on the projected cost of producing NiNCNT-sim 800 °C catalysts in a dedicated factory (CapEx & OpEx method), as visualized through a tornado plot (Fig. 7). The high and low levels used for each parameter were estimated using literature resources and price surveys from similar catalyst production units.[59] Production scale, precursor cost (especially carbon support), and capital expenditure govern the overall catalyst cost, which aligns well with the cost distribution results visualized in the Sankey diagram (Fig. S28).

Notably, the significant impact of the carbon substrate underscores the material-intensive nature of the system, whereby costs scale proportionally with production and thereby limit the benefits typically associated with economies of scale. As a result, while scale-up remains viable, the analysis reveals that meaningful cost reductions can be more effectively achieved through material engineering and process optimization rather than scale alone. This bottom-up cost analysis provides one of the first reported early-stage economic evaluations of an atomically dispersed MNC catalyst for electrochemical systems, offering critical insights into its cost drivers and scale-up viability compared to the precious metal-based alternatives. By quantifying material and processing costs, this work establishes a foundation for future cost optimization and system-level integration. Although the production cost of the synthesized NiNC catalyst is lower than that of Ag-based catalysts, this does not necessarily translate into a reduced CO_2R stack cost, as the overall stack cost is also governed by factors such as catalyst loading, achievable current density, stability, and system-level components (*e.g.*, membrane and balance-of-plant). Moreover, the synthesis of MNC catalysts can involve environmental impacts associated with high-temperature pyrolysis as well as the production and disposal of acidic waste streams during the acid-leaching step, which are steps that are typically not needed when preparing precious metal-based catalysts. To cite an example, Pedersen *et al.*[60] reported that replacing Pt/C with FeNC catalysts decreases the production cost of catalysts for the cathode from $3.41 to 0.79 USD per kW; however, the overall PEMFC stack cost increased from $13.8 to 41.6 USD per kW because of the lower power density output of the resulting stack. An FeNC-based PEMFC would need to achieve a power density of 874 mW cm^{-2} at 0.657 V corresponding to a ~200% improvement over the baseline case (290 mW cm^{-2} at 0.657 V, assuming a catalyst loading of 2.5 mg_{FeNC} cm^{-2} for an 80 kW system), to attain a PEMFC stack cost comparable to that of a Pt/C cathode operating at 1160 mW cm^{-2}.

It should be noted that the present cost analysis primarily focuses on the catalyst synthesis route and evaluates the feasibility of scaling the proposed synthesis method. However, the NiNCNT-sim 800 °C catalyst achieves a partial current density towards CO of 558 mA cm^{-2} at the cell voltage of 3.2 V, which is comparable to the performance of state-of-the-art Ag-based CO_2 electrolyzers operating between 3.2–3.6 V (Table S1). This suggests that NiNC catalysts can deliver similar performance at a substantially lower material cost per unit activity, thereby offering a pathway toward reduced CO_2R stack cost. Future studies are encouraged to incorporate more system-level factors such as catalyst loading, device performance, catalyst stability, and a life cycle analysis that

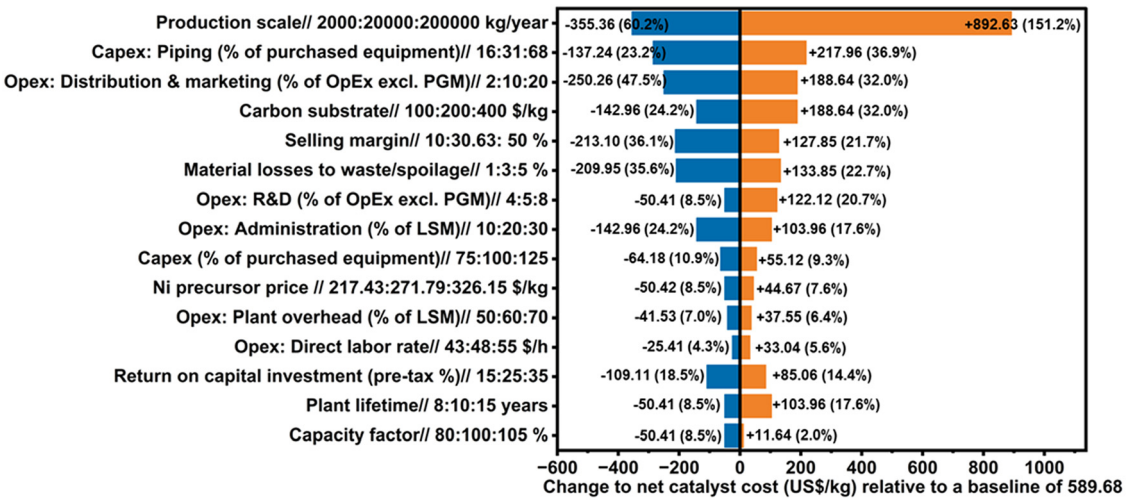

Fig. 7 Tornado plot showing the results of sensitivity analysis. The effect of key input parameters on the net catalyst cost for NiNCNT-sim 800 °C in a dedicated plant at an annual production scale of 2.0×10^4 kg. Input values are listed as low-cost input value: baseline input value: high-cost input value.

considers the environmental impacts associated with the catalyst synthesis to provide a more comprehensive cost assessment.

Conclusions

We uncovered three key factors governing the performance of NiNC catalyst synthesized in this work: the impregnation method of nitrogen precursor, the impact of chelating agent used during synthesis, and the morphology of the carbon support which by extension impacts the morphology of the resulting catalyst layer. Controlled impregnation of the nitrogen precursor through the simultaneous wetness impregnation method alongside the use of glucose as a chelating agent promotes the uniform incorporation of N across the carbon structure and suppresses the agglomeration of Ni ions into clusters. By carefully tuning these parameters, the NiNCNT-sim 800 °C electrode achieved j_{CO} of 558 mA cm^{-2} at 3.2 V with 92% FE towards CO and EE_{CO} of 39%, outperforming previously reported NiNC catalysts and Ag-based benchmarks under comparable MEA conditions. The coupled FIB-SEM tomography with numerical modeling results reveals facilitated CO_2 diffusion in the NiNCNT-sim 800 °C catalyst layer compared to the NiNCB-sim 800 °C electrode, which is associated with the larger interparticle porosity when using CNTs as the catalyst support. Our results underscore that the mass transport in CO_2R is not solely dictated by the intrinsic porosity of the carbon support but is also strongly correlated with the interparticle architecture within the catalyst layer. Achieving optimal CO_2R performance requires an interplay between the nanoscale porosity of the catalyst support, which governs the concentration of electrochemically accessible active sites, and mesoscale interparticle spacing, which controls CO_2 diffusion and transport. Beyond CO_2R electrolyzers, systems limited by gas transport and flooding include any catalyst layers supported on gas diffusion layers or porous transport layers, such as those used in fuel cells, metal–air batteries and water electrolyzers can benefit from the design metrics elucidated herein in terms of engineering the percolated meso/microporosity of the catalyst layer to reduce tortuosity, increase current densities and extend stability. We also estimate the projected purchase cost of the NiNCNT-sim 800 °C as $589 USD per kg, which is substantially lower than Ag-based catalysts, highlighting the industrial potential of this established synthesis method, as well as the demonstration of a quantitative route to identify potential cost advantages for emerging catalyst chemistries. The simultaneous wetness impregnation strategy reported in this work improves metal–nitrogen coordination through improved precursor dispersion, offering a potential strategy for synthesizing atomically dispersed MNC catalysts with different metal centers. Beyond site formation, catalyst layer morphology plays a decisive role in governing CO_2R performance in MEA. Notably, similar Ni–N_x site densities can yield markedly different CO_2R performances due to morphology-driven mass transport limitations (as supported by our FIB-SEM/Multiphysics simulations), highlighting the need to integrate structural and transport considerations in electrode design.

Methods

Materials and chemicals

Chemical precursors used for the catalyst synthesis, electrolyte and electrode preparation were purchased from Sigma-Aldrich. These include melamine, α-D-glucose, high-purity potassium bicarbonate, poly(tetrafluoroethylene) powder, nickel(II) nitrate hexahydrate, hydrochloric acid, isopropyl alcohol, and nitric acid. The multiwall CNTs were purchased from XFNANO (L: 10–20 μm, OD: 4–6 nm). The CB (Ketjen Black) was purchased from Sigma-Aldrich. X37–50 Sustainion anion exchange membrane and iridium oxide anode were purchased from Dioxide Materials. Nafion ionomer D520 solution was also obtained from Ion Power, Inc. The gas diffusion layer (GDL, Sigracet 39 BB) was obtained from Fuel Cell Store. Milli-Q type I ultrapure water (18.2 MΩ cm) was used for all experimental steps.

Catalyst/electrode synthesis

Carbon supports (CB and CNT) were refluxed in 30 wt% HNO_3 solution at 80 °C for 12 h, followed by washing with Milli-Q type I ultrapure water until neutral pH and drying overnight in an oven at 70 °C. For synthesis of the NiNCNT/CB-phys catalysts, 0.15 g of acid-treated carbon support (CNT or CB), 0.11 g of nickel(II) nitrate hexahydrate and 3 g of α-D-glucose were dispersed in 10 ml of Milli-Q type I ultrapure water, and sonicated for 30 min to get a homogenous suspension, followed by stirring for 5 h at room temperature. The slurries were harvested after washing with water and drying at 70 °C. The resulting powder was ground and mixed with 0.75 g of melamine (mass ratio of 1 : 5 with carbon substrate), followed by pyrolysis at various temperatures (700–900 °C) under an Ar atmosphere in a tube furnace for 2 hours at a heating rate of 5 °C min^{-1}. After pyrolysis, the sample was treated with a 5 wt% HCl solution for 2 h (to remove possible Ni clusters), followed by thorough washing with Milli-Q type I ultrapure water until the pH reached 6–7. The resulting material was then dried in an oven at 70 °C overnight. The same procedure was used for the synthesis of NiNCNT/CB-sim samples, with the key difference that all precursors (CNT, glucose, melamine, and the nickel precursor) were co-dispersed in 20 mL of Milli-Q type I ultrapure water and stirred at 80 °C for 5 h to facilitate the dissolution of melamine. The electrodes were also fabricated by dispersing 4 mg of NiNC catalysts in a 2 ml IPA solution containing 4 μL of Nafion ionomer and 0.52 mg of PTFE powder. This ink was drop-casted on the GDL to achieve a catalyst loading of 1 mg cm^{-2}, followed by drying in an oven for 4 hours at 60 °C.

Electrochemical tests

All CO_2R experiments were conducted in a 5 cm^2 MEA cell obtained from Dioxide Materials company with a serpentine channel. Components were compressed using eight bolts

torqued to 40 lb in. An anion exchange membrane (Sustainion X37–50 Grade RT, Dioxide Materials) was inserted between the cathode and the anode (IrO_2 coated on carbon paper). Throughout all experiments, 100 sccm of humidified CO_2 was fed into the cathode flow channels using a mass flow controller, while the anode side was fed with 0.5 M $KHCO_3$ (for stability experiments, 0.1 M $KHCO_3$ solution was used as anolyte). Electrolyte was recirculated at 10 mL min^{-1} with a peristaltic pump. Gaseous products were detected by online gas chromatography (SRI Multigas #5). To estimate the ECSA of the electrodes, the double-layer capacitance of the as-prepared electrodes was measured in 0.5 M $KHCO_3$ electrolyte (Ar-purged). The scan rate was varied from 5 to 100 mV s^{-1} in a non-faradaic potential region using a 3 mm glassy carbon electrode. Faradaic efficiency (FE) for CO and H_2 was calculated based on the equation as follows:

$$FE_i = \frac{z_i \times x_i \times F}{Q} \times 100$$

where z_i is the number of electrons transferred for CO_2R to CO/or H_2, x_i is the number of moles of products, F is the Faraday constant and Q is the total charge passed during the electrolysis. The full cell energy efficiency for CO_2 to CO in MEA was also calculated based on the following equation:

$$EE_{CO} = \frac{1.23 - (-0.10)}{E_{cell}} \times FE_{CO}$$

In this equation, E_{cell} is the cell voltage applied between the cathode and anode in MEA without *iR* correction, FE_{CO} is the measured faradaic efficiency of CO in percentage, −0.10 V *vs.* RHE is the equilibrium potential for CO_2R to CO, and +1.23 V *vs.* RHE accounts for OER equilibrium potential.[61]

Turnover frequencies (TOF) for the production of CO were calculated by:

$$TOF = \frac{FE_{CO} \times I \times M_{Ni}}{\alpha \times F \times m_{cat} \times w_{Ni}}$$

where FE_{CO} is the faradaic efficiency towards CO, I is the total current (equal to partial current density times geometric surface area), M_{Ni} = 58.69 g mol^{-1} is the atomic mass of Ni, α is the number of electrons transferred per mole of gas product (which is 2 for CO), F is the Faraday constant (96 485.3 C mol^{-1}), m_{cat} stands for the catalyst loading on the GDL, and w_{Ni} is the content of Ni in the catalyst (wt%, measured by ICP-OES).

We fitted the near-edge absorption spectra to determine the proportions of the various components by linear combination fitting (LCF). We attempted to fit using a variety of standard samples, including NiO, Ni foil, and NiPc. After testing different combinations, we found that the combination of NiO (13.9%), Ni (20.9%), and NiPc (65.2%) had the best fitting effect, with a R factor of 0.0014 for the NiNCNT-sim 800 °C electrode after stability testing at 200 mA cm^{-2} using pulse chronopotentiometry (3 s at 200 mA cm^{-2}, 1 s at 0 mA cm^{-2}) for 70 hours. On the other hand, a similar analysis on the pristine NiNCNT-sim 800 °C electrode led to NiO (2.0%), Ni (10.6%), and NiPc (87.4%) with an R-factor of 0.0007.

The total site density (sites g^{-1}) was calculated based on the results of ICP-OES and fraction of the Ni present as Ni–N_x using following equation:

$$\text{Site density} = \frac{w_{Ni} \times f_{Ni-N_x} \times N_a}{M_{Ni}}$$

where w_{Ni} is the Ni loading determined from ICP-OES; f_{Ni-N_x} is the fraction of Ni present as Ni–N_x species obtained from LCF using XANES. M_{Ni} is the molar mass of Ni (58.69 g mol^{-1}) and N_a is Avogadro's number (6.022 × 10^{23} sites mol^{-1}). This approach implicitly assumes that all Ni–N_x sites are equally accessible to CO_2 (located at the catalyst surface and thus accessible, rather than buried within the bulk) without mass transport limitations, and therefore this value will overestimate the number of catalytically active sites under operating conditions.

Physicochemical characterization

A thermo Fisher scientific spectra ultra (scanning) transmission electron microscope (STEM) with Cs probe, image correction and a high-brightness Schottky field emitter gun (X-FEG) with ultra-stable monochromator (UltiMono) source was used at 300 kV for transmission electron microscopy (TEM) analysis. A high-angle annular dark field (HAADF) detector and a Ceta camera were used for high-resolution STEM and TEM imaging, respectively. Energy dispersive X-ray (EDX) spectroscopy was done using the ultra-X EDX system at a dwell time of 20 µs per pixel. Electron energy loss (EELS) was also acquired using a CCD camera. Post-filtering of EDX maps was done by averaging every 3 pixels. Data analyses and curation were done using Velox (version 3.10.0.1130-5d766716c0) and Digital Micrograph Software. Specific surface area and pore structures of the catalysts were analyzed by nitrogen physisorption analysis using a Quantachrome ASiQwin instrument. Before the measurements, degassing of the powder samples was done at 110 °C overnight under a continuous flow of N_2 gas. The surface area of the catalysts was estimated using a multipoint Brunauer–Emmett–Teller (BET) model.

X-ray photoelectron spectroscopy (XPS) measurements were performed using a Kratos AXIS Supra spectrometer equipped with a monochromatic Al Kα source (15 mA, 15 kV). All samples were analyzed using the Kratos charge neutralizer system. Survey spectra were acquired with a 300 µm × 700 µm analysis area and a pass energy of 160 eV, while high-resolution spectra were collected over the same area with a pass energy of 20 eV. ICP-OES (Agilent ICP-OES 7900) was used to determine the total Ni contents in the NiNC catalysts. X-ray diffraction (XRD) was performed using a Co Kα radiation source (λ = 1.79 Å) operating at 35 kV and 35 mA. X-ray absorption spectroscopy, comprising X-ray absorption near-edge spectroscopy (XANES) and extended X-ray absorption fine structure (EXAFS) at the Ni K-edge, was performed in total fluorescence yield mode using a silicon drift detector at beamline BL-32A of the Taiwan photon source (TPS), NSRRC. Energy calibration was performed using the first

inflection point of the near-edge region of the Ni foil. Raman spectroscopy was also performed using a Renishaw InVia Raman spectrometer equipped with a 500 mW HeNe laser (λ = 532 nm), operated at 50 mW power with an 1800 L mm^{-1} grating.

FIB-SEM tomography

Focused ion beam-scanning electron microscopy (FIB-SEM) tomography was conducted on the NiNCNT-sim 800 °C and NiNCB-sim 800 °C cathodes using a ThermoFisher Helios 5 UC dual-beam microscope. Near-surface porosity in each unembedded sample was first filled using electron beam deposition of platinum in the FIB at an accelerating voltage of 30 kV and a current of 3.2 nA. This deposition helps reduce the depth of field to a single slice, while providing sufficient imaging contrast for the carbon-based matrix. Each site was then prepared using a standard means for FIB-SEM tomography.[62] Tomography was conducted using Auto Slice-and-View software to obtain 1101 (NiNCB-sim 800 °C) and 1530 (NiNCNT-sim 800 °C) sequential images. Focused ion beam milling of each slice was conducted at 30 kV and 80 pA with an approximate slice thickness of 4 nm (NiNCB-sim 800 °C) or 2 nm (NiNCNT-sim 800 °C). Imaging of each slice was performed using secondary electron signal from a through-lens detector (TLD), with an electron beam accelerating voltage of 1.5–2 kV, a current of 50–1600 pA, a dwell time of 2–3 µs, twofold line averaging, and fourfold frame averaging. Post-process image stack alignment was done in Dragonfly 3D World using a Mutual Info slice alignment algorithm (1% initial translation, 0.01% final translation), and each image stack was then denoised using a 3D Gaussian blur (kernel size = 5, σ = 1.2). 2D UNet convolutional neural networks (CNNs) were trained to segment the images into infilled platinum deposition (as a porosity analog), catalyst material, and background classes using ten manually painted images as a ground truth.[63] The batch size for training was 64, with a patch size of 48, a stride ratio of 0.80, and two-fold data augmentation. Trained CNNs were applied to the full dataset to segment the complete image stack into three classes. The segmented image stacks were then cropped to representative volumes with a size of 250 × 250 × 250 nm, and contour meshes were generated from the pore network segmentations using down-sampling to obtain ~10 000 surface mesh elements in each.

Conflicts of interest

There are no conflicts to declare.

Data availability

The data supporting the findings of this study are available within the manuscript and its supplementary information (SI). Supplementary information includes additional catalyst characterization data, electrochemical measurements, details of FIB-SEM modeling, and supporting figures and tables. See DOI: https://doi.org/10.1039/d6ee00129g.

Acknowledgements

Z. T. acknowledges the financial support from the NSERC Postdoctoral Fellowship. We acknowledge the support of the Government of Canada's New Frontiers in Research Fund (NFRF), CANSTOREnergy project NFRFT-2022-00197. We acknowledge the Canadian Centre for Electron Microscopy (CCEM) at McMaster University for access to instrumentation used to acquire HRTEM/STEM, and FIB-SEM tomography images. We also thank the staff of the McMaster Analytical X-Ray Diffraction Facility for assistance with XRD measurements, and Surface Science Western (SSW) center for XPS analysis. All XAS measurements were performed at beamline BL-32A of the Taiwan Photon Source (TPS). ICP-OES measurements were conducted at the Department of Materials Science and Engineering at McMaster University.

References

1 R. K. Miao, Y. Xu, A. Ozden, A. Robb, C. P. O'Brien, C. M. Gabardo, G. Lee, J. P. Edwards, J. E. Huang, M. Fan and X. Wang, Electroosmotic flow steers neutral products and enables concentrated ethanol electroproduction from CO2, *Joule*, 2021, **5**(10), 2742–2753. Available from: https://www.cell.com/joule/fulltext/S2542-4351(21)00397-4.

2 A. R. W Woldu, A. G. Yohannes, Z. Huang, P. Kennepohl, D. Astruc, L. Hu and X. C. Huang, Experimental and Theoretical Insights into Single Atoms, Dual Atoms, and Sub-Nanocluster Catalysts for Electrochemical CO_2 Reduction (CO_2RR) to High-Value Products, *Adv. Mater.*, 2024, **36**(52), 2414169. Available from: https://onlinelibrary.wiley.com/doi/10.1002/adma.202414169.

3 P. Li, Y. Mao, H. Shin, Q. Yang, X. Cheng, Y. Li, K. Li, H. Yu, R. Mulder, W. K. Pang and H. Jin, Tandem amine scrubbing and CO_2 electrolysis *via* direct piperazine carbamate reduction, *Nat. Energy*, 2025, 1–12. Available from: https://www.nature.com/articles/s41560-025-01869-8.

4 W. Lai, Y. Qiao, Y. Wang and H. Huang, Stability Issues in Electrochemical CO_2 Reduction: Recent Advances in Fundamental Understanding and Design Strategies, *Adv. Mater.*, 2023, **35**(51), 2306288. Available from: https://onlinelibrary.wiley.com/doi/10.1002/adma.202306288.

5 IEA [Internet]. [cited 2025 Jul 30]. CO_2 Emissions – Global Energy Review 2025 – Analysis. Available from: https://www.iea.org/reports/global-energy-review-2025/co2-emissions.

6 S. Wang, Z. Qian, Q. Huang, Y. Tan, F. Lv, L. Zeng, C. Shang, K. Wang, G. Wang, Y. Mao and Y. Wang, Industrial-Level CO_2 Electroreduction Using Solid-Electrolyte Devices Enabled by HighLoading Nickel Atomic Site Catalysts, *Adv. Energy Mater.*, 2022, **12**(31), 2201278. Available from: https://onlinelibrary.wiley.com/doi/10.1002/aenm.202201278.

7 C. Zhu, G. Wu, A. Chen, G. Feng, X. Dong, G. Li, S. Li, Y. Song, W. Wei and W. Chen, Selective CO_2 electroreduction to multicarbon products exceeding 2 A cm^{-2} in strong acids *via* a hollow-fiber Cu penetration electrode, *Energy Environ. Sci.*, 2024, **17**(2), 510–517. Available from: https://pubs.rsc.org/en/content/articlehtml/2005/kn/d3ee02867d.

8 M. Ma and B. Seger, Rational Design of Local Reaction Environment for Electrocatalytic Conversion of CO_2 into Multicarbon Products, *Angew. Chem., Int. Ed.*, 2024, **63**(23), e202401185. Available from: https://onlinelibrary.wiley.com/doi/10.1002/anie.202401185.

9 F. Jiao, J. Li, X. Pan, J. Xiao, H. Li, H. Ma, M. Wei, Y. Pan, Z. Zhou, M. Li and S. Miao, Selective conversion of syngas to light olefins, *Science*, 2016, **351**(6277), 1065–1068. Available from: https://www.science.org/doi/10.1126/science.aaf1835.

10 Z. Teimouri, N. Abatzoglou and A. K. Dalai, Insights to the reaction kinetics of Fischer–Tropsch synthesis using an integral system over Cu-Mo promoted Fe catalyst, *Fuel*, 2024, **360**, 130512. Available from: https://www.sciencedirect.com/science/article/pii/S0016236123031265?via%3Dihub.

11 L. Xing, H. Jiang, X. Tian, H. Yin, W. Shi, E. Yu, V. J. Pinfield and J. Xuan, Combining machine learning with multi-physics modelling for multi-objective optimisation and techno-economic analysis of electrochemical CO_2 reduction process, *Carbon Capture Sci. Technol.*, 2023, **9**, 100138. Available from: https://www.sciencedirect.com/science/article/pii/S2772656823000428.

12 J. Osorio-Tejada, M. Escriba-Gelonch, R. Vertongen, A. Bogaerts and V. Hessel, CO_2 conversion to CO *via* plasma and electrolysis: a techno-economic and energy cost analysis, *Energy Environ. Sci.*, 2024, **17**(16), 5833–5853. Available from: https://pubs.rsc.org/en/content/articlehtml/2024/ee/d4ee00164h.

13 C. Yan, N. Li and G. A. Ozin, EES Catalysis [Internet]. 2023 [cited 2025 Jan 21]. Available from: https://scholar.archive.org/work/eukaf3y2z5dd3ki2f5khzjfine/access/wayback/https://pubs.rsc.org/en/content/articlepdf/2024/ey/d3ey00155e.

14 M. Zeng, W. Fang, Y. Cen, X. Zhang, Y. Hu and B. Y. Xia, Reaction Environment Regulation for Electrocatalytic CO_2 Reduction in Acids, *Angew. Chem., Int. Ed.*, 2024, **63**(26), e202404574. Available from: https://onlinelibrary.wiley.com/doi/10.1002/anie.202404574.

15 M. Sassenburg, M. Kelly, S. Subramanian, W. A. Smith and T. Burdyny, Zero-Gap Electrochemical CO2 Reduction Cells: Challenges and Operational Strategies for Prevention of Salt Precipitation, *ACS Energy Lett.*, 2023, **8**(1), 321–331. Available from: https://pubs.acs.org/doi/10.1021/acsenergylett.2c01885.

16 T. Zheng, K. Jiang, N. Ta, Y. Hu, J. Zeng, J. Liu and H. Wang, Large-scale and highly selective CO2 electrocatalytic reduction on nickel single-atom catalyst, *Joule*, 2019, **3**(1), 265–278. Available from: https://www.cell.com/joule/fulltext/S2542-4351(18)30506-3.

17 X. Su, X. F. Yang, Y. Huang, B. Liu and T. Zhang, Single-Atom Catalysis toward Efficient CO_2 Conversion to CO and Formate Products, *Acc. Chem. Res.*, 2019, **52**(3), 656–664. Available from: https://pubs.acs.org/doi/10.1021/acs.accounts.8b00478.

18 M. Li, H. Wang, W. Luo, P. C. Sherrell, J. Chen and J. Yang, Heterogeneous Single-Atom Catalysts for Electrochemical CO_2 Reduction Reaction, *Adv. Mater.*, 2020, **32**(34), 2001848. Available from: https://onlinelibrary.wiley.com/doi/10.1002/adma.202001848.

19 L. Zhao, Y. Zhang, L. B. Huang, X. Z. Liu, Q. H. Zhang, C. He, Z. Y. Wu, L. J. Zhang, J. Wu, W. Yang and L. Gu, Cascade anchoring strategy for general mass production of high-loading single-atomic metal-nitrogen catalysts, *Nat. Commun.*, 2019, **10**(1), 1278. Available from: https://www.nature.com/articles/s41467-019-09290-y.

20 L. Gong, D. Zhang, C. Y. Lin, Y. Zhu, Y. Shen, J. Zhang, X. Han, L. Zhang and Z. Xia, Catalytic Mechanisms and Design Principles for Single-Atom Catalysts in Highly Efficient CO_2 Conversion, *Adv. Energy Mater.*, 2019, **9**(44), 1902625. Available form: https://onlinelibrary.wiley.com/doi/abs/10.1002/aenm.201902625.

21 A. Bagger, W. Ju, A. S. Varela, P. Strasser and J. Rossmeisl, Electrochemical CO_2 Reduction: A Classification Problem, *ChemPhysChem*, 2017, **18**(22), 3266–3273. Available from: https://onlinelibrary.wiley.com/doi/abs/10.1002/cphc.201700736.

22 N. Wang, H. Li, H. Wang, H. Yang, Z. Ren and R. Xu, Temperature-Induced Low-Coordinate Ni Single-Atom Catalyst for Boosted CO_2 Electroreduction Activity, *Small*, 2023, **19**(35), 2301469. Available from: https://onlinelibrary.wiley.com/doi/10.1002/smll.202301469.

23 Y. E. Kim, Y. N. Ko, B. S. An, J. Hong, Y. E. Jeon, H. J. Kim, S. Lee, J. Lee and W. Lee, Atomically Dispersed Nickel Coordinated with Nitrogen on Carbon Nanotubes to Boost Electrochemical CO_2 Reduction, *ACS Energy Lett.*, 2023, **8**(8), 3288–3296. Available from: https://pubs.acs.org/doi/10.1021/acsenergylett.3c00933.

24 C. Jia, Y. Zhao, S. Song, Q. Sun, Q. Meyer, S. Liu, Y. Shen and C. Zhao, Highly Ordered Hierarchical Porous Single-Atom Fe Catalyst with Promoted Mass Transfer for Efficient Electroreduction of CO_2, *Adv. Energy Mater.*, 2023, **13**(37), 2302007. Available from: https://onlinelibrary.wiley.com/doi/10.1002/aenm.202302007.

25 S. Fu, B. Izelaar, M. Li, Q. An, M. Li, W. de Jong and R. Kortlever, The effect of carbon supports on the electrocatalytic performance of Ni-NC catalysts for CO2 reduction to CO, *Nano Energy*, 2025, **133**, 110461. Available from: https://www.sciencedirect.com/science/article/pii/S2211285524012138.

26 R. M. Arán-Ais, D. Gao and B. Roldan Cuenya, Structure- and Electrolyte-Sensitivity in CO_2 Electroreduction, *Acc. Chem. Res.*, 2018, **51**(11), 2906–2917. Available from: https://pubs.acs.org/doi/10.1021/acs.accounts.8b00360.

27 K. M. Barcelos, K. S. Oliveira and L. A. Ruotolo, Insights on the role of interparticle porosity and electrode thickness on capacitive deionization performance for desalination, *Desalination*, 2020, **492**, 114594. Available from: https://www.sciencedirect.com/science/article/pii/S0011916420312728.

28 S. Gupta, S. Zhao, O. Ogoke, Y. Lin, H. Xu and G. Wu, Engineering Favorable Morphology and Structure of Fe-N-C

Oxygen-Reduction Catalysts through Tuning of Nitrogen/Carbon Precursors, *ChemSusChem*, 2017, **10**(4), 774–785. Available from: https://chemistry-europe.onlinelibrary.wiley.com/doi/10.1002/cssc.201601397.

29 Intratec | Reliable & Independent Information about Commodities [Internet]. [cited 2026 Mar 11]. Available from: https://www.intratec.us/.

30 S. C. Yan, Z. S. Li and Z. G. Zou, Photodegradation Performance of g-C_3N_4 Fabricated by Directly Heating Melamine, *Langmuir*, 2009, **25**(17), 10397–10401. Available from: https://pubs.acs.org/doi/10.1021/la900923z.

31 Z. Ma, B. Wang, X. Yang, C. Ma, W. Wang, C. Chen, F. Liang, N. Zhang, H. Zhang, Y. Chu and Z. Zhuang, P-Block Aluminum Single-Atom Catalyst for Electrocatalytic CO_2 Reduction with High Intrinsic Activity, *J. Am. Chem. Soc.*, 2024, **146**(42), 29140–29149. Available from: https://pubs.acs.org/doi/10.1021/jacs.4c11326.

32 W. Hua, H. Sun, L. Lin, Q. Mu, B. Yang, Y. Su, H. Wu, F. Lyu, J. Zhong, Z. Deng and Y. Peng, A hierarchical Single-Atom Ni-N3-C catalyst for electrochemical CO_2 reduction to CO with Near-Unity faradaic efficiency in a broad potential range, *Chem. Eng. J.*, 2022, **446**, 137296. Available from: https://www.sciencedirect.com/science/article/pii/S1385894722027851?casa_token=Zi9ryJYT4fgAAAAA:ZMe8U7NTipZJwY5B4hBFPhjP4D3D4YliBZqNGXYinuRde3H1WPfim62iyDdkgWk1JvC1vM05Lg.

33 S. Wang, Z. Qian, Q. Huang, Y. Tan, F. Lv, L. Zeng, C. Shang, K. Wang, G. Wang, Y. Mao and Y. Wang, Industrial-Level CO_2 Electroreduction Using Solid-Electrolyte Devices Enabled by High-Loading Nickel Atomic Site Catalysts, *Adv. Energy Mater.*, 2022, **12**(31), 2201278. Available from: https://onlinelibrary.wiley.com/doi/10.1002/aenm.202201278.

34 M. Zhang, X. Wang, J. Ding, C. Ban, Y. Feng, C. Xu and X. Zhou, Realizing ampere-level CO_2 electrolysis at low voltage over a woven network of few-atom-layer ultralong silverene nanobelts with ultrahigh aspect ratio by pairing with formaldehyde oxidation, *Nanoscale*, 2024, **16**(14), 7076–7084. Available from: https://pubs.rsc.org/en/content/articlehtml/2024/nr/d4nr00361f.

35 B. Endrődi, A. Samu, E. Kecsenovity, T. Halmágyi, D. Sebök and C. Janáky, *Operando* cathode activation with alkali metal cations for high current density operation of water-fed zero-gap carbon dioxide electrolysers, *Nat. Energy*, 2021, **6**(4), 439–448. Available from: https://idp.nature.com/authorize/casa?redirect_uri=https://www.nature.com/articles/s41560-021-00813-w&casa_token=jLzIhwIDMp4AAAAA:4hKhNxn7cCLVe-ApmJX-80qKcBVW5x-d2P0533mHc5-maM5T76k_K61XzGbuonaaH2S-quMc81bDABvm.

36 S. Hao, A. Elgazzar, N. Ravi, T. U. Wi, P. Zhu, Y. Feng, Y. Xia, F. Y. Chen, X. Shan and H. Wang, Improving the operational stability of electrochemical CO_2 reduction reaction *via* salt precipitation understanding and management, *Nat. Energy*, 2025, **10**(2), 266–277. Available from: https://idp.nature.com/authorize/casa?redirect_uri=https://www.nature.com/articles/s41560-024-01695-4&casa_token=XF1WM1fDegkAAAAA:zeEvdDexoFZA0ipmreqr9sAN8b4jyOG9GqaKq86XGXsvEE_80YTK9oU8hcqbSdNI5LJTVcznQ84xbe88.

37 J. Disch, S. Ingenhoven and S. Vierrath, Bipolar Membrane with Porous Anion Exchange Layer for Efficient and Long-Term Stable Electrochemical Reduction of CO_2 to CO, *Adv. Energy Mater.*, 2023, **13**(38), 2301614. Available from: https://advanced.onlinelibrary.wiley.com/doi/10.1002/aenm.202301614.

38 T. Haas, R. Krause, R. Weber, M. Demler and G. Schmid, Technical photosynthesis involving CO_2 electrolysis and fermentation, *Nat. Catal.*, 2018, **1**(1), 32–39. Available from: https://idp.nature.com/authorize/casa?redirect_uri=https://www.nature.com/articles/s41929-017-0005-1&casa_token=h7IqDuSN3xcAAAAA:G1ChSOaTLrBjCOc4LeOXyQRmvA-iwGB1op8oE7bi5NnZoAVE4CC96au3rK__cFwawVrtDbouO8AGGQmP.

39 C. Lim, S. Kim, J. H. Song, M. H. Han, Y. J. Ko, K. Y. Lee, J. Y. Choi, W. H. Lee and H. S. Oh, Breaking the current limitation of electrochemical CO_2 reduction *via* a silica-hydroxide cycle, *Energy Environ. Sci.*, 2024, **17**(17), 6215–6224. Available from: https://pubs.rsc.org/en/content/articlehtml/2024/ee/d4ee00448e.

40 D. Wakerley, S. Lamaison, F. Ozanam, N. Menguy, D. Mercier, P. Marcus, M. Fontecave and V. Mougel, Bio-inspired hydrophobicity promotes CO_2 reduction on a Cu surface, *Nat. Mater.*, 2019, **18**(11), 1222–1227. Available from: https://idp.nature.com/authorize/casa?redirect_uri=https://www.nature.com/articles/s41563-019-0445-x&casa_token=6GYDANd5PIcAAAAA:UlosghJV3WuURcuNzHC9EsJKZVQd2ZpwrZ49yqLjEA2LfrdHIUQ5znMj7maSNhxii1-nKyH1j8FSssO0.

41 Y. Wu, H. Rabiee, X. S. Zhao, G. Wang and Y. Jiang, Insights into electrolyte flooding in flexible gas diffusion electrodes for CO_2 electrolysis: from mechanisms to effective mitigation strategies, *J. Mater. Chem. A*, 2024, 14206–14228. Available from: https://pubs.rsc.org/en/content/articlehtml/2024/ta/d4ta01994f.

42 Q. Xu, A. Xu, S. Garg, A. B. Moss, I. Chorkendorff, T. Bligaard and B. Seger, Enriching Surface-Accessible CO_2 in the Zero-Gap Anion-Exchange-Membrane-Based CO_2 Electrolyzer, *Angew. Chem., Int. Ed.*, 2023, **62**(3), e202214383. Available from: https://onlinelibrary.wiley.com/doi/10.1002/anie.202214383.

43 Y. L. Chung, S. Kim, Y. Lee, D. T. Wijaya, C. W. Lee, K. Jin and J. Na, Pulsed electrolysis for CO_2 reduction: Techno-economic perspectives, *iScience*, 2024, **27**(8), 110383. Available from: https://www.cell.com/iscience/fulltext/S2589-0042(24)01608-0.

44 J. Masa, W. Xia, M. Muhler and W. Schuhmann, On the Role of Metals in Nitrogen-Doped Carbon Electrocatalysts for Oxygen Reduction, *Angew. Chem., Int. Ed.*, 2015, **54**(35), 10102–10120. Available from: https://onlinelibrary.wiley.com/doi/abs/10.1002/anie.201500569.

45 J. Masa, A. Zhao, W. Xia, Z. Sun, B. Mei, M. Muhler and W. Schuhmann, Trace metal residues promote the activity of supposedly metal-free nitrogen-modified carbon catalysts for the oxygen reduction reaction, *Electrochem. Commun.*, 2013, **34**, 113–116. Available form: https://www.sciencedirect.com/science/article/pii/S1388248113002154.

46 S. Fu, M. Li, W. De Jong and R. Kortlever, Tuning the Properties of N-Doped Biochar for Selective CO_2 Electroreduction to CO, *ACS Catal.*, 2023, **13**(15), 10309–10323. Available from: https://pubs.acs.org/doi/10.1021/acscatal.3c01773.

47 S. Inkoua, C. Li, Y. Shao, H. Lin, M. Fan, L. Zhang, S. Zhang and X. Hu, Co-hydrothermal carbonization of fruit peel with sugars or furfural impacts structural evolution of hydrochar, *Ind. Crops Prod.*, 2023, **193**, 116221. Available from: https://www.sciencedirect.com/science/article/pii/S0926669022017046?casa_token=AUSAPUj4XJ0AAAAA:44T2vI1sim187SYhkzhyRlxjCrds8KvgJ-3SsM3gNf0T5uoaSLIgESeXguaZufFk1J97AdSkAAPb.

48 G. Wu, N. H. Mack, W. Gao, S. Ma, R. Zhong, J. Han, J. K. Baldwin and P. Zelenay, Nitrogen-doped graphene-rich catalysts derived from heteroatom polymers for oxygen reduction in nonaqueous lithium–O2 battery cathodes, *ACS Nano*, 2012, **6**(11), 9764–9776. Available from: https://pubs.acs.org/doi/full/10.1021/nn303275d.

49 G. Wu and P. Zelenay, Nanostructured Nonprecious Metal Catalysts for Oxygen Reduction Reaction, *Acc. Chem. Res.*, 2013, **46**(8), 1878–1889. Available from: https://pubs.acs.org/doi/10.1021/ar400011z.

50 X. Zhang, Y. Wang, M. Gu, M. Wang, Z. Zhang, W. Pan, Z. Jiang, H. Zheng, M. Lucero, H. Wang and G. E. Sterbinsky, Molecular engineering of dispersed nickel phthalocyanines on carbon nanotubes for selective CO_2 reduction, *Nat. Energy*, 2020, **5**(9), 684–692. Available from: https://www.nature.com/articles/s41560-020-0667-9.

51 M. A. McArthur, L. Jorge, S. Coulombe and S. Omanovic, Synthesis and characterization of 3D Ni nanoparticle/carbon nanotube cathodes for hydrogen evolution in alkaline electrolyte, *J. Power Sources*, 2014, **266**, 365–373. Available from: https://www.sciencedirect.com/science/article/pii/S0378775314007198.

52 Y. Sun, F. Bai, J. Liu, S. Sun, Y. Mao, X. Liu, Y. Huang and Y. Chen, Identification of Degradation Reasons for a CO_2 MEA Electrolyzer Using the Distribution of Relaxation Times Analysis, *J. Phys. Chem. Lett.*, 2024, **15**(35), 9122–9128. Available from: https://pubs.acs.org/doi/10.1021/acs.jpclett.4c02024.

53 Y. Zhao, Z. Shi, F. Li, C. Jia, Q. Sun, Z. Su and C. Zhao, Deciphering Mesopore-Augmented CO2 Electroreduction over Atomically Dispersed Fe–N-doped Carbon Catalysts, *ACS Catal.*, 2024, **14**(6), 3926–3932. Available from: https://pubs.acs.org/doi/10.1021/acscatal.3c05144.

54 T. Moore, X. Xia, S. E. Baker, E. B. Duoss and V. A. Beck, Elucidating Mass Transport Regimes in Gas Diffusion Electrodes for CO_2 Electroreduction, *ACS Energy Lett.*, 2021, **6**(10), 3600–3606. Available from: https://pubs.acs.org/doi/10.1021/acsenergylett.1c01513.

55 A. Senocrate, F. Bernasconi, D. Rentsch, K. Kraft, M. Trottmann and A. Wichser, *et al.*, Importance of Substrate Pore Size and Wetting Behavior in Gas Diffusion Electrodes for CO_2 Reduction, *ACS Appl. Energy Mater.*, 2022, **5**(11), 14504–14512. Available from: https://pubs.acs.org/doi/10.1021/acsaem.2c03054.

56 N. G. Moreno, M. C. Molina, D. Gervasio and J. F. P. Robles, Approaches to polymer electrolyte membrane fuel cells (PEMFCs) and their cost, *Renewable Sustainable Energy Rev.*, 2015, **52**, 897–906. Available from: https://www.sciencedirect.com/science/article/pii/S1364032115008047.

57 Estimates | CatCost [Internet]. [cited 2025 May 12]. Available from: https://catcost.chemcatbio.org/catalyst-estimate.

58 F. Chang, G. Zhan, Z. Wu, Y. Duan, S. Shi, S. Zeng, X. Zhang and S. Zhang, Technoeconomic Analysis and Process Design for CO_2 Electroreduction to CO in Ionic Liquid Electrolyte, *ACS Sustainable Chem. Eng.*, 2021, **9**(27), 9045–9052. Available from: https://pubs.acs.org/doi/10.1021/acssuschemeng.1c02065.

59 I. M. Anekwe, E. E. Lora, K. A. Subramanian, A. Kozlov, S. Zhang, B. Oboirien and Y. M. Isa, Techno-economic and life-cycle analysis of single-step catalytic conversion of bioethanol to fuel blendstocks over Ni-doped HZSM-5 zeolite catalyst, *Energy Convers. Manage.: X*, 2024, **22**, 100529. Available from: https://www.sciencedirect.com/science/article/pii/S2590174524000072.

60 A. Pedersen, J. Pandya, G. Leonzio, A. Serov, A. Bernardi, I. E. Stephens, M. M. Titirici, C. Petit and B. Chachuat, Comparative techno-economic and life-cycle analysis of precious versus non-precious metal electrocatalysts: the case of PEM fuel cell cathodes, *Green Chem.*, 2023, **25**(24), 10458–10471. Available from: https://pubs.rsc.org/en/content/articlehtml/2023/gc/d3gc03206j.

61 S. Nitopi, E. Bertheussen, S. B. Scott, X. Liu, A. K. Engstfeld, S. Horch, B. Seger, I. E. Stephens, K. Chan, C. Hahn and J. K. Nørskov, Progress and Perspectives of Electrochemical CO2 Reduction on Copper in Aqueous Electrolyte, *Chem. Rev.*, 2019, **119**(12), 7610–7672. Available from: https://pubs.acs.org/doi/10.1021/acs.chemrev.8b00705.

62 M. D. Uchic, L. Holzer, B. J. Inkson, E. L. Principe and P. Munroe, Three-Dimensional Microstructural Characterization Using Focused Ion Beam Tomography, *MRS Bull.*, 2007, **32**(5), 408–416. Available from: https://link.springer.com/10.1557/mrs2007.64.

63 O. Ronneberger, P. Fischer and T. Brox, U-Net: Convolutional Networks for Biomedical Image Segmentation, in *Lecture Notes in Computer Science*, Springer International Publishing, Cham, 2015, pp. 234–241. Available from: https://link.springer.com/10.1007/978-3-319-24574-4_28, DOI: 10.1007/978-3-319-24574-4_28.